RESEARCH ARTICLE

ADVANCED FUNCTIONAL MATERIALS
www.afm-journal.de

Silver—Gallium Nano-Amalgamated Particles as a Novel, Biocompatible Solution for Antibacterial Coatings

Tien Thanh Nguyen, Pengfei Zhang, Jingwei Bi, Ngoc Huu Nguyen, Yen Dang, Zhaoning Xu, Hao Wang, Neethu Ninan, Richard Bright, Tuyet Pham, Chung Kim Nguyen, Ylias Sabri, Manh Tuong Nguyen, Jitraporn Vongsvivut, Yunpeng Zhao, Krasimir Vasilev,* and Vi Khanh Truong**

Bacterial infections account for countless deaths globally. Antibiotics are the primary countermeasure; however, the alarming spread of antibiotic-resistant strains necessitates alternative solutions. Silver and silver compounds have emerged as promising antibacterial agents. However, issues related to cytotoxicity and genotoxicity of silver remain concern. To overcome these challenges, this proposes an easy-to-control and straightforward method to synthesize novel Silver—gallium (Ag—Ga) nano-amalgamated particles. Gallium liquid metal (GaLM) is used to facilitate the galvanic deposition of silver nanocrystals (Ag) on oxide layer. The GaLM not only serves as a carrier for silver through the galvanic replacement process, but also provides a controlled-release mechanism for silver, in this way improving biocompatibility, reducing inflammation, and stimulating bone growth. Notably, Ag—Ga suspensions can be conveniently deposited by spray-coating on a range of devices and material surfaces, effectively eliminating pathogenic bacteria with efficacy comparable to that of silver ions. In vivo studies in rat models affirm the antibacterial capabilities, especially against methicillin-resistant *Staphylococcus aureus and Escherichia coli*, when placed on implants such as titanium rods and magnesium discs. Furthermore, Ag—Ga promotes bone matrix formation and collagen growth without eliciting an inflammatory response, indicating a major promise for coatings on a wide variety of biomedical devices and materials.

1. Introduction

Biomedical device-associated infections (BDAIs) pose a significant global challenge for both patients and healthcare systems.[1] Despite the implementation of stringent disinfection management and aseptic surgical environments, BDAI infection rates remain between 2% and 10% in developed countries.[2] Due to inequalities in healthcare resources and practices, infection rates in developing nations can escalate up to 15%.[3] BDAIs can lead to severe complications, including disability, mortality, and greatly increased healthcare expenditure. In the United States, there are >100 000 cases of orthopedic fracture and reconstruction devices-related infections, which clearly asserts the magnitude of the issues.[4] A 2017 Australian study found that among 3705 primary hip and knee replacements, the two-year infection rate was 1.7%, with 0.6% occurring within the first four weeks and 1.1% between 4 weeks and 2 years.[5] Moreover, ≈6% of individuals with orthopedic implant infections necessitate admission to intensive

---

T. T. Nguyen, N. H. Nguyen, Y. Dang, N. Ninan, R. Bright, T. Pham,
M. T. Nguyen, K. Vasilev, V. K. Truong
Biomedical Nanoengineering Laboratory
College of Medicine and Public Health
Flinders University
Adelaide, SA 5042, Australia
E-mail: krasimir.vasilev@flinders.edu.au;
vikhanh.truong@flinders.edu.au

The ORCID identification number(s) for the author(s) of this article can be found under https://doi.org/10.1002/adfm.202310539

DOI: 10.1002/adfm.202310539

T. T. Nguyen
College of Medicine and Pharmacy
Tra Vinh University
Tra Vinh 87000, Viet Nam

P. Zhang, J. Bi, Y. Zhao
Department of Orthopedics
Qilu Hospital of Shandong University
Jinan, Shandong 250012, P. R. China
E-mail: lwwzyp@email.sdu.edu.cn

P. Zhang, J. Bi
Cheeloo College of Medicine
Shandong University
Jinan, Shandong 250012, P. R. China

Z. Xu
Department of Nursing
The First Affiliated Hospital of Shandong First Medical University &
Shandong Provincial Qianfoshan Hospital
Jinan, Shandong 250012, P. R. China

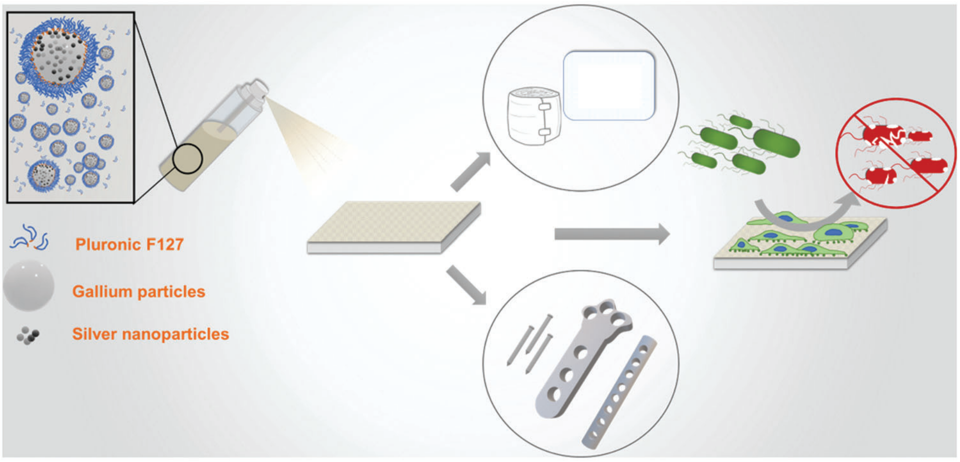

Scheme 1. Schematic illustration of the formulation of Ag—Ga nano-amalgamated particles suspension and application on medical devices.

care units associated with a heightened mortality rate of up to 4.6%.[6] Apart from the immense patient suffering, which often leads to amputations or even death, the cost of revising these infections exceeds US$100 000, including the cost of the implant.[7] These statistics highlight the pressing need for enhanced infection prevention measures, improved resource accessibility, and innovative interventions to alleviate the burden of these infections on a global scale.

Traditional antibiotic therapies demonstrate limitations in effectively resolving BDAIs, as relapse after treatment remains a substantial concern. High-risk infections such as these in the case of bone implants are closely linked to patients with compromised immune systems and the formation of biofilms on the implant surface.[6,8] The latter requires significantly higher doses of antibiotics, up to 1000-fold, for effective treatment.[9] Hence, there is an urgent need for innovative solutions to help reduce device colonization by bacteria and establish long-term protection against infections.

The antibacterial properties of silver (Ag) have been well-established and utilized in various medical devices, including wound dressings such as Acticoat (Smith&Nephew),[10] Tegaderm,[11] GranuFoam Silver,[12] and catheters like Bardex Silver,[13] Palindrome,[14] and ARROW CVCs.[15] The growing challenge of antibiotic-resistant bacteria, coupled with the positive outcomes observed with Ag-coated dressings and catheters, has stimulated further research and development efforts to incorporate silver into orthopedic implants. Recent advancements have led to the market introduction of Ag-coated megaprostheses, including METS Silver Agluna System (Stanmore Implants), MUTARS (Implantcast GmbH), and PorAg (Waldemar Link), demonstrating promising results in reducing infection rates.[16] The mechanisms underlying the antibacterial properties of silver have been reported in many studies. These include: 1) inducing lysis in bacterial cell membranes due to the electrostatic interactions between the positively charged Ag ions and negatively charged bacterial cell membranes[17]; 2) disrupting the respiratory chain and hindering adenosine triphosphate synthesis[17,18]; and AgNPs inhibiting the replication processes by binding to bacterial DNA.[19] However, challenges remain in addressing early inflammatory responses and enhancing the integration of silver-coated implants with bone tissue (osteointegration).[20] Recent findings of bacterial resistance to silver have raised concerns about the long-term effectiveness of Ag-based antimicrobial treatments.[21] There are also reports suggesting that high concentrations of silver can damage mammalian cell membranes,[22] as well as cause genotoxic and cytotoxic damage to structures such as the human organ [23] and glioblastoma cells.[24] Another study reported that high concentrations of Ag ions can suppress the immune system.[25]

In particular, it has been observed that repeated exposure to AgNPs can induce resistance in Gram-negative bacteria, such as various strains of *Escherichia coli*, without involving genetic alterations.[21,26] This resistance is attributed to phenotypic changes that result in the suppression of flagellum protein synthesis. Interestingly, investigations have shown that strains resistant to AgNPs did not simultaneously develop resistance to Ag ions, suggesting that bacterial cells may respond differently to distinct forms of silver.[27] It is noteworthy that certain bacteria possess specific genes, for example, the *sil* genes (e.g., *sil*E, *sil*P, and *sil*S), which contribute to resistance against Ag ions by facilitating efflux, sequestration, or reduction of silver.[28] Further research is required to unravel the underlying mechanisms of Ag resistance and provide alternative or complementary strategies to combat this threat.

Gallium liquid metal (GaLM) has emerged as a promising alternative for various medical applications due to its unique properties and associated advantages. Previous studies have

---

H. Wang
Department of Orthopedics
Shandong Provincial Hospital Affiliated to Shandong First Medical University
Jinan, Shandong 250012, P. R. China

C. K. Nguyen, Y. Sabri
School of Engineering
RMIT University
Melbourne, VIC 3000, Australia

J. Vongsvivut
Infrared Microspectroscopy Beamline
ANSTO Australian Synchrotron
Clayton, VIC 3168, Australia

demonstrated that Ga exhibits moderate antimicrobial activity against a wide range of pathogens, making it a versatile solution for addressing bacterial infections.[29] Importantly, Ga ions possess a distinct mechanism of action that disrupts bacterial iron metabolism, thereby reducing the potential for the development of bacterial resistance. Clinical trials involving gallium nitrate have shown efficacy in treating bacterial infections in human subjects.[30] Notably, Ga nanoparticles can induce anti-inflammatory responses without interfering with the iron homeostasis pathway in immune cells. Also, Ga nanoparticles were demonstrated to possess low cytotoxicity,[31] while gallium nitrate and citrate were found to promote bone growth. **Scheme 1**.[32]

In this study, we aim to employ gallium liquid metal (GaLM) particles as carriers for silver to achieve a synergistic Silver─gallium (Ag─Ga) nano-amalgamated particles through the galvanic replacement process to achieve enhanced antimicrobial properties and low toxicity. The synthesis process, as shown in Scheme 1, is designed to transform Ag^+ into Ag nanocrystals through galvanic replacement, with silver nanocrystals robustly adhering to the GaLM particle surfaces. Crucially, GaLM demonstrates an ability to markedly mitigate silver toxicity through forming silver nanocrystals on GaLM oxide surface, while amplifying antimicrobial potency, attenuating inflammation, and bolstering osseointegration. We have applied the Ag─Ga particle suspension as a sprayable solution on various medical materials, including bioabsorbable magnesium alloys and titanium. In vivo evaluations validate robust antibacterial properties, including eliminating pathogens such as methicillin-resistant *S. aureus* and *E. coli*. Furthermore, Ag─Ga particle coatings support bone-mimetic matrix and collagen development without eliciting an inflammatory response.

2. Results and Discussion

2.1. Synthesis and Characterization of Ag─Ga Suspension

Silver─gallium (Ag─Ga) nano-amalgamated particles were synthesized by mixing Ga droplets suspension with $AgNO_3$ and F-127 solutions. First, Ga particle suspension was obtained using probe ultrasonication methods as previously described.[33] A suspension of gallium (Ga) was created by introducing around 57 mg of liquid gallium into 10 mL of Milli-Q (MQ) water. The mixture was then subjected to probe sonication for varying durations ranging from 15 to 25 min. Due to the effects of heat on the formation of crystalline gallium oxyhydroxide (GaOOH) (rod-shape),[33] probe sonication was performed in an ice bath, and then mixed with $AgNO_3$ solution using a vortex mixer before the addition of F-127 (**Figure 1**a). The structure of the Ga particles, enveloped by an oxide layer, is schematically depicted in Figure 1b. Each Ga particle consists of a liquid Ga core surrounded by native surface oxides.[34] This unique composition gives the Ga particles an adhesive capacity, which can be attributed to the combined effects of the enveloping surface oxides and the malleability of the liquid core.[29] The size of the Ga particles (refer to **Table 1**; Figure S1, Supporting Information) reveals that as the ultrasonication period extends from 15 to 35 min, the Ga particles tend to be of reduced average sizes and exhibit a more uniform size spread. However, no notable change in size distribution was observed between the 25 to 35 min mark. Therefore, 25-min time point was selected for synthesizing GaLM for the experiments discussed later.

The diagram shown in Figure 1c outlines the proposed strategy for producing Ag─Ga through galvanic replacement. When silver nitrate solution is introduced to a Ga suspension, the Ag─Ga particles form spontaneously through the galvanic replacement process, represented by Equation (1).

$$\mathrm{Ga\,(l)} + 3\mathrm{Ag}^+\,\mathrm{(aq)} \rightarrow 3\mathrm{Ag\,(s)} + \mathrm{Ga}^{3+}\,\mathrm{(aq)}\,,\; E^0 = 1.328\ \mathrm{V} \qquad (1)$$

We propose, as depicted in Figure 1c, that when Ga particles interact with an $AgNO_3$ solution, silver nanocrystals emerge and become affixed onto the oxide layer of the GaLM droplets. This event can be better understood by referencing the theory of Mott─Cabrera on standard reduction potentials, detailing the chemical reaction typically present on metal oxides.[35] This concept suggests that metals inherently develop a ≈3 nm thick oxide layer on their exteriors, which forms spontaneously because of electronic transitions.[36] In our case, the reaction progression is likely due to the presence of a thin metal oxide layer and the pronounced difference in standard reduction potentials between the electron donor (GaLM) and the electron acceptor (silver ions).[37] Hence, a reaction that is thermodynamically spontaneous transpires on the GaLM oxide surface, influenced by the standard reduction potential (with Ga^{3+}/Ga and Ag^+/Ag values being −0.529 and 0.799 V against the standard hydrogen electrode (SHE), respectively).[38] The outcome is the formation and attachment of silver nanocrystal to the GaLM oxide surface.

Once the Ag─Ga particles have been generated, a modest quantity of F-127 is introduced to the solution to establish a stabilizing coating around the Ag─Ga particles. F-127 is a non-toxic polymer that has been approved by FDA for biomedical applications.[39] Extensively researched for its applications in cellular and drug delivery, F-127 possesses advanced characteristics like minimal toxicity, temperature-triggered gelation in reverse, the ability to encapsulate drugs, and the capacity to form a gel even at low concentrations.[40] Therefore, we selected F-127 as a safe surfactant to maintain the stability of the Ag─Ga suspension as without it the Ga suspension would rapidly precipitate (Figure 1d).[33]

To better visualize the Ag nanocrystals attached to the oxide layer of the Ga particles, the Ag─Ga particles were washed with water to remove excess F-127. Both the Ga and Ag─Ga particles, were subsequently inspected using Scanning Electron Microscope (SEM). The SEM images showed that the Ga only suspension produced mostly smooth and spherical particles (Figure 1e) while Ag─Ga suspension contained rough spherical particles with bound crystal structure (determined to be solid silver) on the surface of the Ga particles (Figure 1f). Interestingly, the interaction between the Ga particles and Ag ions appears to become more pronounced as the concentration of $AgNO_3$ increases. As evidenced in Figure 1g, the Ga particles have undergone substantial depletion, leading to the emergence of pronounced surface indentations, and coupled with an increase in the crystalline particle count. Therefore, the structure of the Ga particles undergoes notable changes with increasing the concentration of silver ions (Figure S2, Supporting Information).

The presence of Ag nanocrystals binding to Ga particles was further investigated using other advanced techniques. Scanning

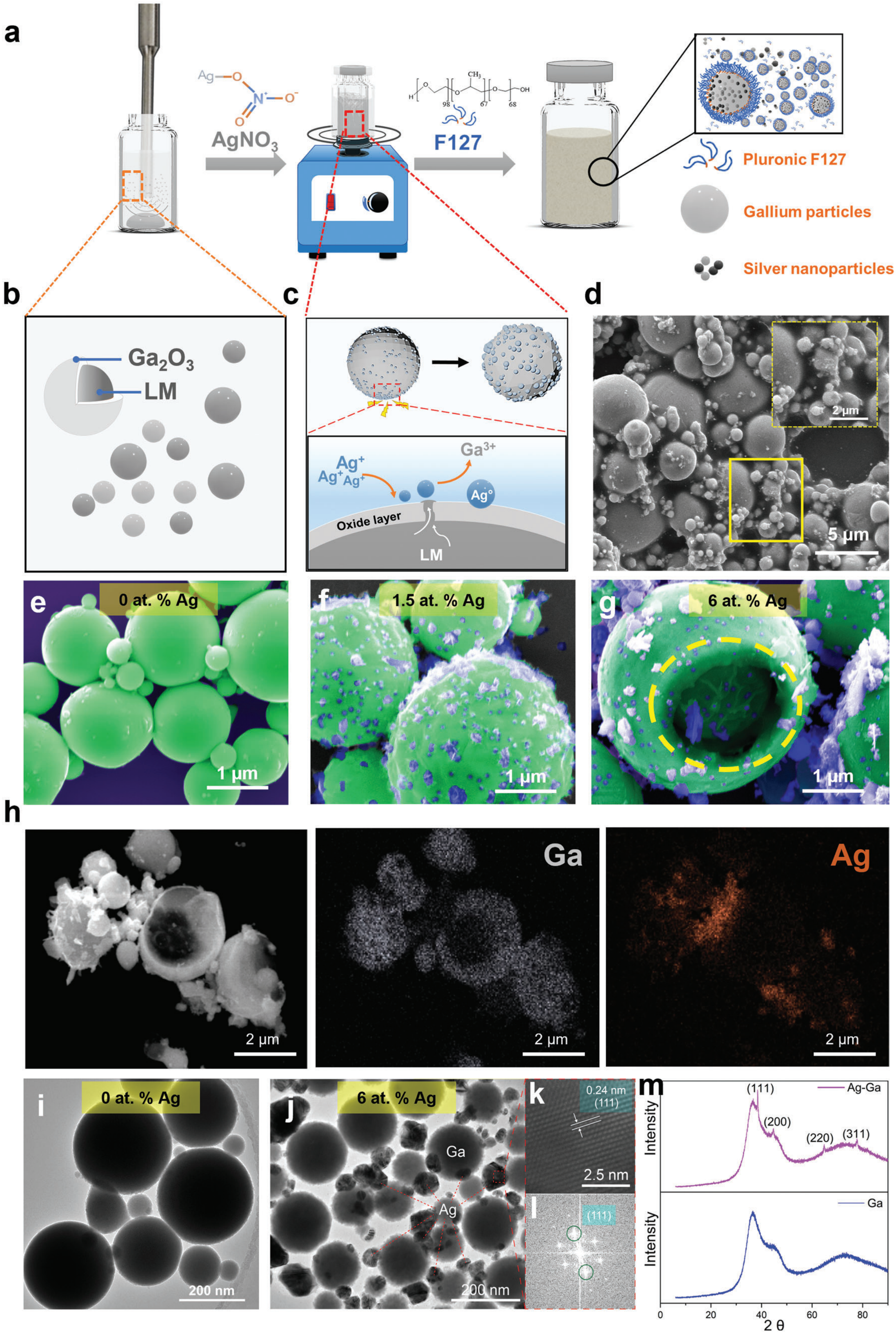
a
AgNO$_3$
F127
Pluronic F127
Gallium particles
Silver nanoparticles
b
Ga$_2$O$_3$
LM
c
Ag$^+$
Ag$^+$Ag$^+$
Ga^{3+}
Ag^0
Oxide layer
LM
d
2 μm
5 μm
e
0 at. % Ag
1 μm
f
1.5 at. % Ag
1 μm
g
6 at. % Ag
1 μm
h
2 μm
Ga
2 μm
Ag
2 μm
i
0 at. % Ag
200 nm
j
6 at. % Ag
Ga
Ag
200 nm
k
0.24 nm
(111)
2.5 nm
l
(111)
m
Intensity
(111)
(200)
(220)
(311)
Ag-Ga
Intensity
Ga
0
20
40
60
80
2 θ

Table 1. The dimensions of Ga and Ag—Ga particles for different sonication time points.

Sonication time [min]	Ga particles		Ag—Ga particles	
	Average diameter [nm]	Standard deviation [nm]	Average diameter [nm]	Standard deviation [nm]
15	343.93	235.75	331.73	249.27
20	318.57	275.17	307.27	272.03
25	306.70	243.50	295.83	214.53
30	297.73	209.30	281.93	229.40
35	274.33	178.60	257.43	194.27

electron microscopy-energy dispersive X-ray spectroscopy (SEM-EDS) was utilized to determine the presence of silver on the surface of the GaLM particles in the Ag—Ga nano-amalgam, showing the presence of Ag and Ga in the sample analysis (Figure 1h). Transmission electron microscopy (TEM) images of Ag—Ga revealed alterations in the Ga particles. In contrast to the uniform circular mass observed in Ga particles alone (Figure 1i), the configuration of Ga particles in Ag—Ga was no longer uniform or circular (Figure 1j). Furthermore, the substance within the gallium turns porous and exhibits reduced density, highlighting the changes in atomic concentration within the Ga particles after interaction with silver nitrate. Also, the distinction between the Ga droplets (larger particles) and the tiny nanoparticles adhering to the Ga particles' surface is evident due to the variations in their atomic structures. Moreover, a high-resolution TEM (HRTEM) image and its relevant Fast Fourier-transform (FFT) images also revealed a d-spacing of 0.24 nm (Figure 1k), matching well with the (111) plane of the face-centered cubic structure of silver (Figure 1l).[41] The presence of solid silver was consistently verified using X-ray diffraction (XRD) techniques. In Figure 1m, the XRD patterns of Ag—Ga are presented, which were produced from the interaction of Ga droplets with Ag ions. Peaks identified at 2θ values of 38.45°, 44.76°, 64.79°, and 77.72° align with the (111), (200), (220), and (311) planes of Ag crystals.[42] These peaks are indicative of a face-centered cubic lattice formation and its inherent crystalline structure, as indexed in JCPDS-04–0783.[43] These observations align with the TEM findings, where Ag nanocrystals were observed to form on the surface of Ga particles. This provides compelling evidence that the nanoparticles found around Ga particles are silver nanocrystals, formed from the reaction between Ga (in liquid form) and $AgNO_3$ at 37 °C. Although no obvious formation of Ag—Ga intermetallic compounds was detected by the TEM and XRD analysis, the presence of these bimetallic systems may affect the release of Ag cations and will be the focus of future studies.

In the previous research conducted by our team, we explored the crystallization phenomenon occurring through the galvanic replacement process involving gallium and copper (Cu).[29] This process led to the generation of Cu crystals on Ga-coated fabrics when it was immersed in high concentrations of $CuSO_4$. The noted repercussion of this chemical reaction was a systematic augmentation in the dimensions of Cu crystals, which have been substantiated to exhibit robust and enduring antibacterial characteristics.[29] This present study focuses on the synthesis of Ag nanocrystals in the presence of Ga.[23,44] In this study, we used 6% Ag in Ag—Ga nano-amalgamated particles for our antimicrobial, biocompatibility, and in vivo evaluation.

X-ray photoelectron spectroscopy (XPS) was utilized to examine the elemental compositions and chemical states on the synthesized particle surfaces. **Figure 2** displays the XPS results for Ga droplets with varying Ag concentrations (0, 1.5, 3, 4, and 6 at.%). In all samples, except for pure Ga droplets, silver was discernible through doublet peaks, specifically Ag $3d_{5/2}$ and Ag $3d_{3/2}$, at binding energies of 367.5 and 373.4 eV, respectively.[45] Gallium presence was marked by peaks at binding energies of 1118.5 and 1145.2 eV, corresponding to Ga $2p_{3/2}$ and Ga 2 $p_{1/2}$, respectively.[44] Importantly, the distinct signals from both silver and gallium elements were minimally affected by the Pluronic surfactant (F-127). This indicates that the polymer layer encasing the Ag—Ga might be thinner than 10 nm, the detection threshold of XPS. Furthermore, the C 1*s* peak was deconvoluted into three distinct peaks. The dominant binding energy peaks at 286.5 and 285 eV correspond to the C—O and C—C bonds, respectively, and were detected across all samples. These peaks confirm the incorporation of F-127 on the particle surface. The O—C bond peak, found at 533 eV, had the highest intensity under the O 1*s* peaks. The signal for the O—Ga bond was seen at a binding energy of 531 eV. Collectively, the XPS data suggest that both Ga and Ag—Ga droplets are enveloped by a thin surfactant layer (F-127), which could potentially inhibit further gallium oxidation. The XPS results showed that the Ga and Ag—Ga droplets could be covered by a thin layer of F-127 which might have prevented the further oxidation of gallium.

2.2. Antimicrobial Properties of Ag—Ga

The antibacterial activity of the Ag—Ga nano-amalgamated particles was assessed against *Staphylococcus aureus* and *Pseudomonas aeruginosa*. These represent two frequently encountered bacteria in BDAIs.[46] These bacteria also serve as representatives for Gram-positive and Gram-negative types and their distinct cellular structures. When examined via the disc diffusion method, the Ga particle suspensions exhibited a relatively weak antibacterial

Figure 1. a) A schematic depiction of the preparation of Ag—Ga nanoparticle suspension. b) The morphology of gallium particles including gallium oxide coating (outside) and gallium liquid metal (inside) in solution. c) Schematics of galvanic replacement GaLM particles with Ag ion. d) The Ag—Ga formulation coated by F-127. Post-colored SEM micrograph of Ga particles e) and Ag—Ga suspension with 1.5% Ag f) and 6% Ag g), scale bar is 1 µm. h) Energy dispersive X-ray spectroscopy (EDX) cross-section mapping of 6% Ag in Ag—Ga suspension synthesized from direct probe sonication, scale bar is 2 µm. TEM image of Ga particles i) and Ag—Ga suspension with 6% Ag j), the red dotted line showing the presence of Ag while the smooth spherical shape presented the Ga particles; k) high-resolution TEM (HRTEM) image and l) its fast Fourier transform (FTT) image, revealing the detection of silver structure in the suspension, scale bars are 200 and 2.5 nm. m) The XRD findings indicate the presence of Ag nanoparticles, as evidenced by the diffraction peaks associated with the (111), (200), (220), and (311) planes. The humps observed in XRD spectra of Ga are from liquid Ga and glass substrates.

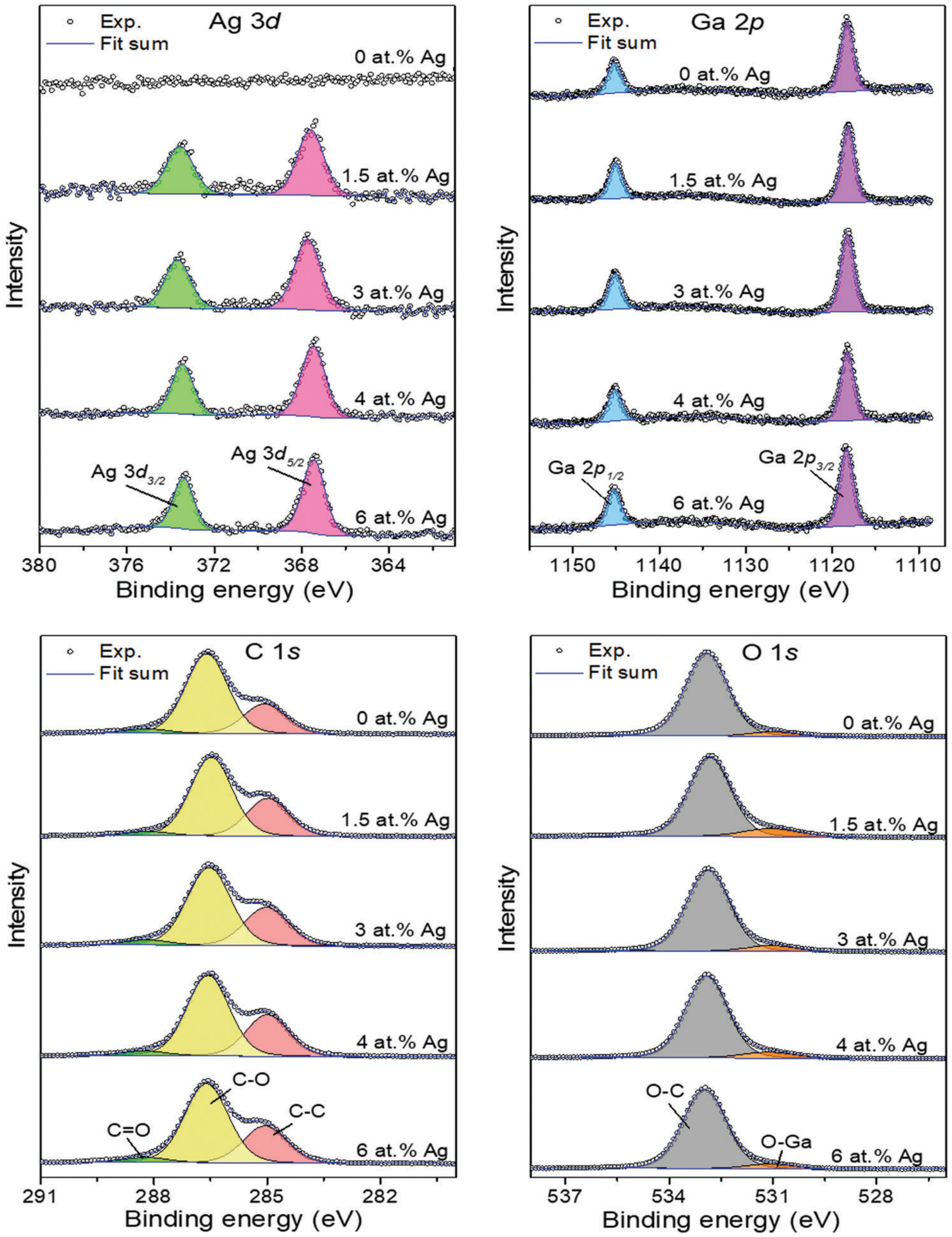

Figure 2. XPS spectra of the chemical composition of Ag—Ga suspension showing the presence of chemical elements in the Ag—Ga synthesis with different silver concentrations.

zone with diameters of 8.56 mm ± 0.40 and 7.23 mm ± 0.25 for *P. aeruginosa* and *S. aureus*, respectively, shown in Figure S4 (Supporting Information). The antibacterial potential was significantly amplified when Ga particles were reacted with $AgNO_3$ to form Ag—Ga nano-amalgamated particles. The inhibition zones formed by the Ag—Ga particles were 11.2 mm ± 0.25 for *P. aeruginosa* and 10.2 mm ± 0.26 for *S. aureus*. Additionally, as indicated in **Figure 3**a,b, Ag—Ga particles displayed impressive efficiency in eradicating bacteria upon contact, achieving 99% elimination rates for both *S. aureus* and *P. aeruginosa* at 16 µg Ag and 176 µg Ga cm^{-2} concentrations. Notably, the antibacterial ability of Ga particles was substantially augmented, especially toward *S. aureus* when integrated with silver nanocrystals on the metal oxide exterior.

The viability of the pathogen cells on silicon wafers coated with Ag—Ga and Ga was accessed using confocal laser scanning microscopy (CLSM). The results are shown in Figure 3c. For this study, we employed Live/Dead fluorescent staining (with green signifying live cells and red for dead cells) following a 24-h period of interaction with either the control or the nanoparticle coatings. In the case *S. aureus*, only a slight reduction in the intensity of the green fluorescence (corresponding to live bacteria) was observed on the Ga particles coated surface. In comparison, near complete death of *S. aureus* cells was observed on the Ag—Ga

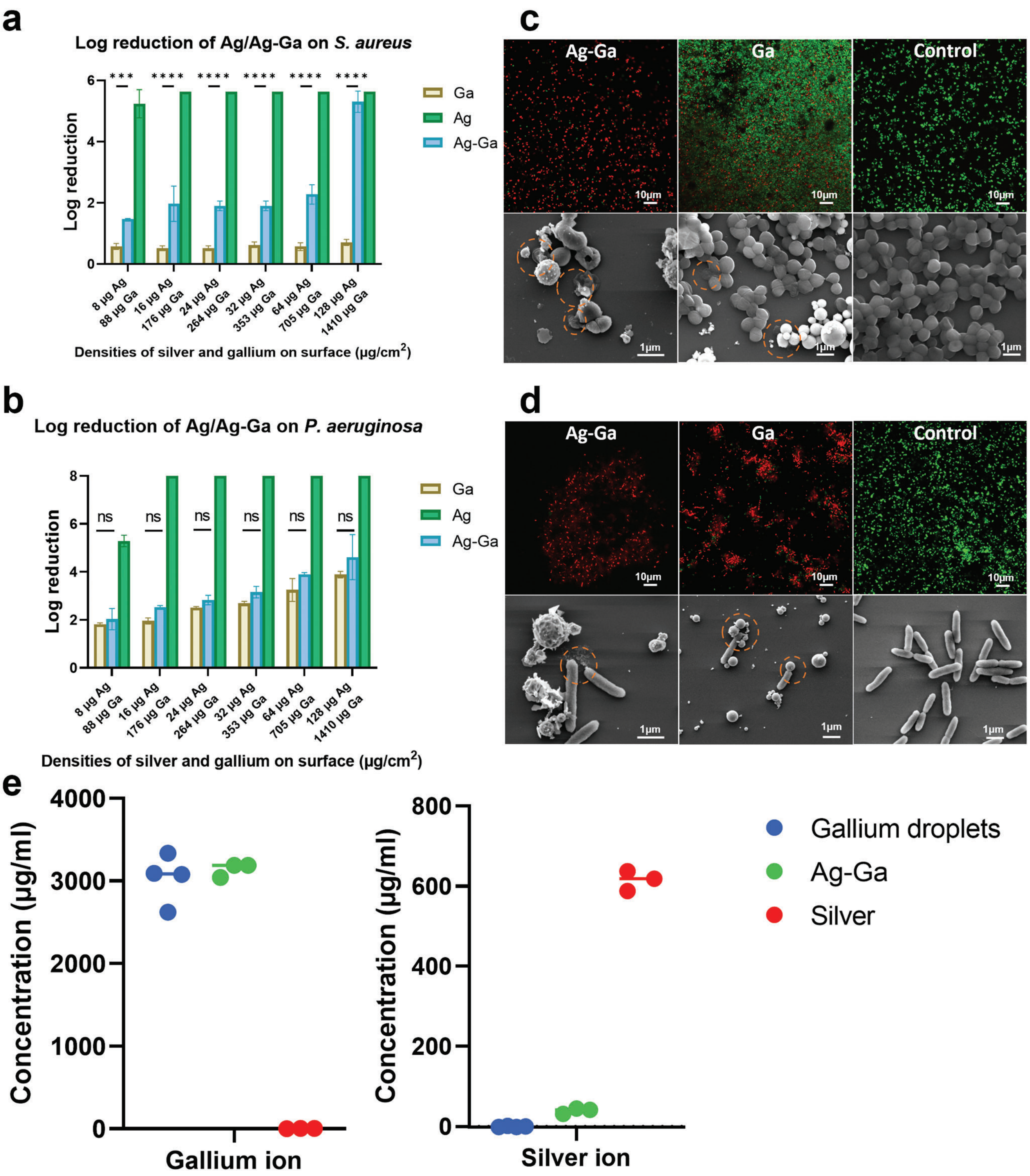

Figure 3. Antibacterial efficacies of Ag—Ga particles. Log reduction of Ag^+ (denoted as Ag), Ag—Ga, and Ga against a) *S. aureus* and b) *P. aeruginosa* after 18 h of incubation. Error bar represents mean ± s.d., $n = 3$, $^{***}p < 0.001$, $^{**}p < 0.01$, $^{*}p < 0.05$. CLSM (green: viable cells; and red: dead cells) and SEM images of c) *S. aureus* and d) *P. aeruginosa* on the surfaces coated Ga (176 µg cm^2), Ag—Ga (16 µg Ag + 176 µg Ga cm^{-2}), and Ag (16 µg cm^{-2}). Scale bars are 10 µm (CLSM) and 1 µm (SEM). e) The concentrations of Ag^+ and Ga^{3+} released from coatings of Ag, Ag—Ga, and Ga in TSB media after 24 h incubation at 37 °C. Values represent mean ± s.d., $n = 3$.

coated surface, accompanied by intense red fluorescence denoting dead bacteria.

On the other hand, the efficiency in eradicating *P. aeruginosa* by both the Ag—Ga and Ga coatings was nearly comparable (as depicted in Figure 3d). This can be attributed to the potent bactericidal effect of Ga against *P. aeruginosa* documented in the scientific literature.[29,47]

The antimicrobial action of Ag—Ga composite nanoparticles was investigated through membrane potential and Reactive Oxygen Species (ROS) assays. Figure S6a (Supporting Information) demonstrates that exposure to Ag—Ga-coated surfaces led to membrane potential shifts in both tested pathogenic bacteria, evidenced by green fluorescence in their cells. These alterations can be attributed to the Ag—Ga nanoparticles adhering to the bacterial cell membrane, as depicted in SEM images of Figures 3c,d. Such adherence can disrupt the integrity of membrane, leading to wrinkling, tearing, and the formation of holes. This causes significant changes in bacterial cell morphology and membrane functions, ultimately leading to cell inactivation. Additionally, the antimicrobial properties of Ag—Ga are also due to its ability to generate ROS. These are highly reactive molecules and free radicals formed from molecular oxygen. As shown in Figure S6b.(Supporting Information), intracellular ROS were evident in both bacterial types when exposed to Ag—Ga coated surfaces. Notably, the fluorescent intensity of ROS in *S. aureus* was higher compared to that in *P. aeruginosa*. ROS can cause cellular damage by oxidizing DNA, RNA, carbohydrates, proteins, and lipids, leading to cell death.[48]

SEM imaging provided further support by demonstrating a reduced number of bacteria on both Ag—Ga and Ga-coated surfaces. Notably, the Ag—Ga coating surface revealed pronounced damage to the cell membranes, visibly disrupting the original rod-like morphology of *P. aeruginosa* and the spherical morphology of *S. aureus* (Figure 3c,d). The nanoparticles impact significantly changes the bacterial cell structure, resulting in cell deactivation. This finding aligns well with published studies, which show that bacterial deformation arose due to the adherence between the cell membrane and Ga particles.[49] Additionally, the disruption of bacterial morphology is notably enhanced when silver nanoparticles are present on the surface of the Ga particles. The Ag—Ga combination demonstrates a heightened efficacy against *S. aureus* compared to Ga particles alone.

In the Ag—Ga system, Ga particles function as a reservoir for silver formed through a reaction between the Ga droplets and silver nitrate. This suggests a potential for a moderated release of silver ions into the surrounding environment. Indeed, based on the inductively coupled plasma mass spectroscopy (ICP-MS) analysis presented in Figure 3e, the release of silver ions from surfaces coated with Ag—Ga in a tryptic soy broth (TSB) environment >24 h at 37 °C was ≈14 times lower than that from surfaces coated with Ag ion. Simultaneously, the release of gallium ions from the Ga and Ag—Ga coated samples was similar, with concentrations ≈3000 μm. As a result, given its inherent ability to encapsulate and release silver ions at a controlled rate, the Ag—Ga system is proficient in eradicating bacterial cells and can sustain this advantage for extended durations. Furthermore, the prolonged and calibrated release of silver ions could potentially mitigate the cytotoxic effect associated with high concentrations of silver ions.

To evaluate the surface antibacterial efficacy of the Ag—Ga solution, an area of TSA (tryptic soy agar), pre-coated with the two types of pathogenic bacteria used in this work, was spray-coated with Ag—Ga particles and then incubated for 24 h. It is worth highlighting that the regions treated with the Ag—Ga solution developed prominent antibacterial zones (Figure S7, Supporting Information). Conversely, those areas treated with Ga or AgNPs only do not possess clear antibacterial zones (Figure S7, Supporting Information).

2.3. The Intricate Biochemical Alterations Instigated Induced by Ag—Ga and Ga on Bacteria

We conducted the cutting-edge synchrotron macro-attenuated total reflection ATR-FTIR micro-spectroscopy to delve into the intricate biochemical shifts triggered by Ag—Ga and Ga particles in two pathogenic bacteria, that is, the Gram-positive *Staphylococcus aureus* and the Gram-negative *Pseudomonas aeruginosa*. This technique enabled us to identify shifts in the structural molecules of the bacteria. The synchrotron macro-ATR-FTIR analysis process is shown in Figure S8 (Supporting information). We conducted principal component analysis (PCA) to identify distinct changes in the ATR-FTIR spectra between bacteria treated with Ag—Ga and Ga suspensions, and untreated bacteria, as shown in **Figure 4**.

For *S. aureus*, biochemical modifications following interactions with Ga and Ag—Ga particles were evident through PC-1 loadings of 89% and 92% of the spectral variation, respectively. These data suggest that there were substantial biochemical shifts. Peaks associated with PC-1, utilized to determine the most distinct wavenumbers and their chemical components between treated and untreated bacteria, emerged from the divergence in PCA loading. The intensity of these loading peaks provides insight into the degree of difference, with heightened intensities reflecting more significant variation. Central peaks are illustrated in Figure 4a,b, while the associated biochemical compounds are detailed in Table S1 (Supporting Information). Figure 4a shows the recorded peak intensities span bands indicative of the lipid zone, amide I, and polysaccharides. This points to changes in chemical structures tied to bacterial membranes and proteins.[50] Changes of particular interest occur in the polysaccharide structures of bacteria, evidenced by the elevated intensity of peaks within this zone. Concurrently, the engagement of Ga particles with *S. aureus* resulted in notable shifts within the lipid and polysaccharide domains, as highlighted by the peak intensities in these sectors (Figure 4b). The potential of Ag—Ga and Ga particles to bring about biochemical structural changes was similarly seen in *P. aeruginosa*, with PC-1 loading values of 98% and 99%, respectively (Figures 4c,d). These shifts are discernible by the occurrence of peaks in regions associated with lipids, proteins, and polysaccharides. Notably, in the lipid area of both samples, two prominent groups of peaks corresponding to modifications in the methyl/methylene groups (2922 and 2858 cm^{-1}) of the phospholipids of cell membrane were detected.[51] These modifications are likely due to the cell membrane damage caused by the impact of Ga-Ag and Ga particles (SEM images in Figure 3c,d).

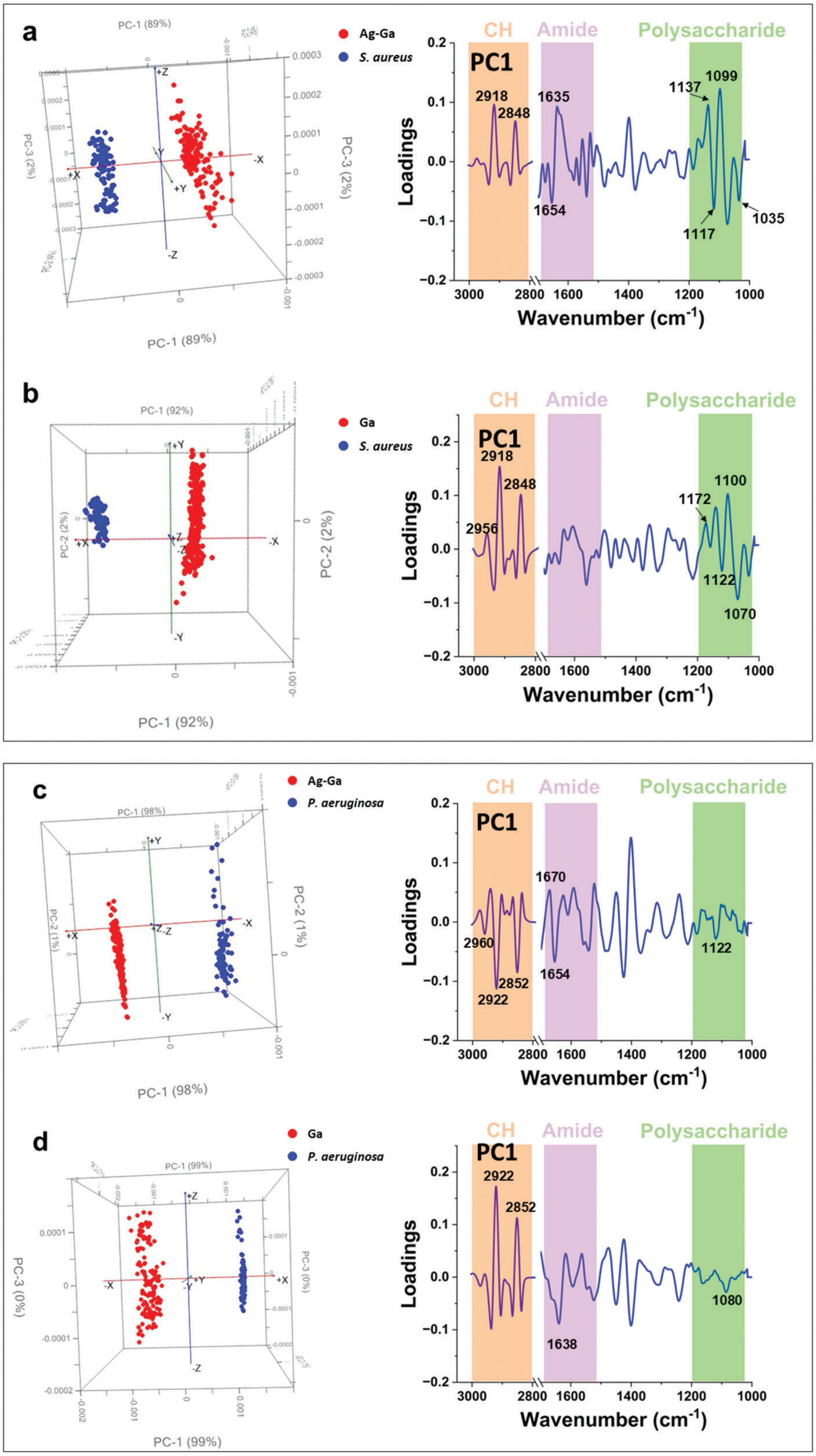

Figure 4. Principal component analysis (PCA) of untreated and treated *S. aureus* cells. Comparative PCA score plots (left side) and PCA loading spectra correlations PC-1 (right side) for *S. aureus* treated by Ag—Ga a) and Ga b) with *S. aureus*. The left side displays the comparative PCA score plots, whereas the right features the PCA loading spectra correlations for PC-1, which illustrates a comparison of *P. aeruginosa* when treated with Ag—Ga c) and Ga d) to untreated *P. aeruginosa*. The peaks of interest and their corresponding assignments are summarized in Table S1 (Supporting Information).

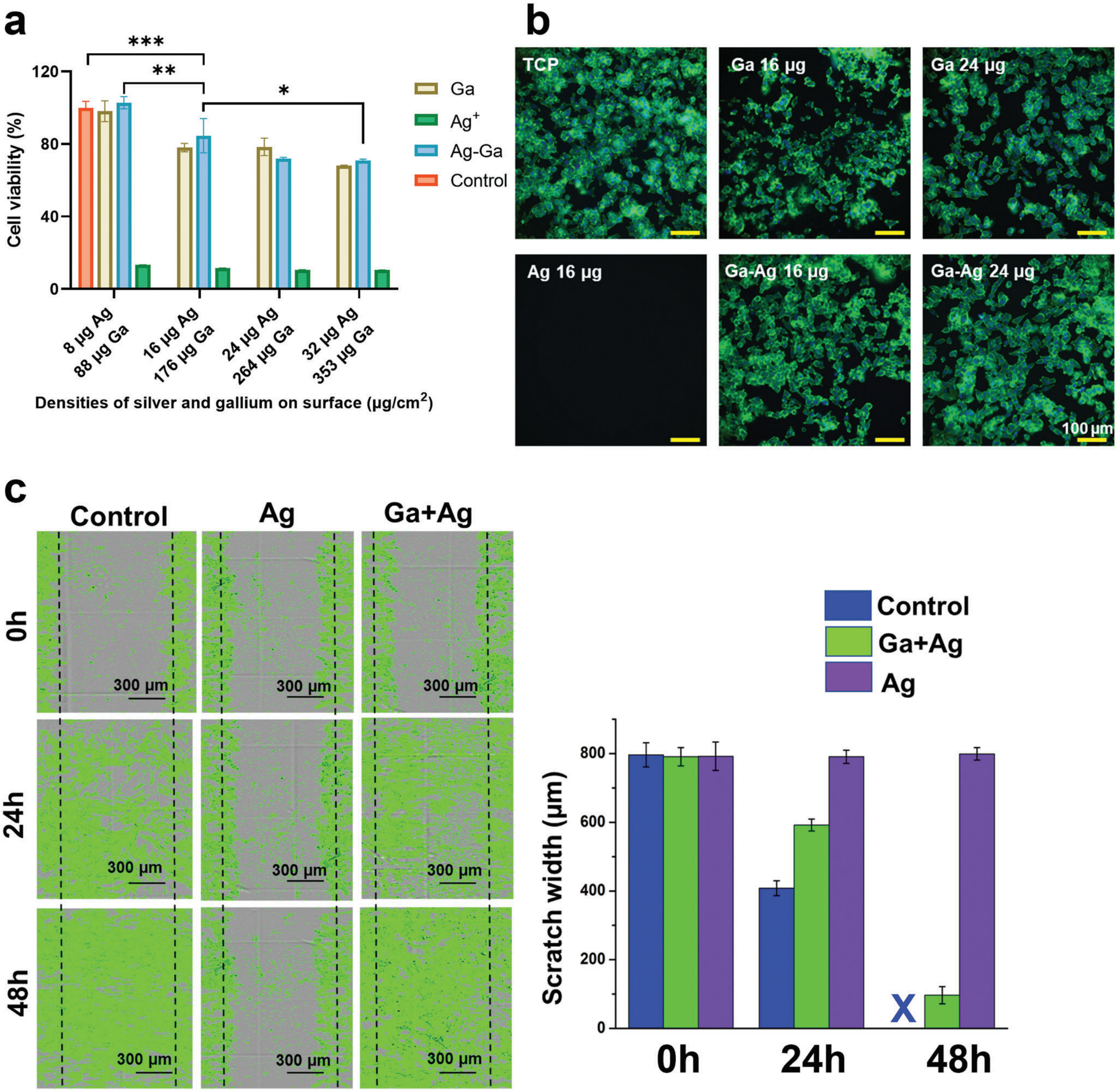

Figure 5. Evaluating the cytotoxicity and wound healing ability of the coatings containing Ga, Ag, Ag—Ga. CCK8 assay assessing the viability of HaCaT cells a) incubated in DMEM with Ag/Ag—Ga for 24 h. b) CLSM images of HaCaT cells following 24 h incubation with silicon surfaces coated Ag—Ga, Ag and Ga (Green: Phalloidin; Blue: DAPI). c) Cell migration assay of Ag and Ag—Ga conditioned medium and control medium for 0, 24 and 48 h, demonstrating increased cell motility and proliferation in the case of cells incubated in Ag—Ga conditioned medium and control medium. Mean ± s.d, $n = 3$, $^{***}p < 0.001$, $^{**}p < 0.01$, $^{*}p < 0.05$.

2.4. Biocompatibility and Cell Migration Assays

To investigate the effects of Ag, Ga, and Ag—Ga suspensions on cell viability, we carried out the cell count kit −8 (CCK8) assay with different densities of suspensions (8, 16, 24, 32 µg cm^{-2} of Ag; 88, 176, 264, 353 µg cm^{-2} of Ga; Ag—Ga respectively) in HaCaT cells after 24 h of incubation. As shown in **Figure 5**a, Ag significantly reduced cell growth at all densities of the suspension with a rate of 11%; conversely, Ga slightly reduced cell growth with an acceptable rate (<30%), according to ISO 10993:5:2009 standards.[52] Surprisingly, Ag—Ga successfully reduced cell cytotoxicity of Ag from 11% in the Ag group to 84% in the Ag—Ga group.

Furthermore, confocal laser scanning microscopy (CLSM) was utilized to visualize cells incubated on Ag—Ga, Ag and Ga, and compared to controls (silicon wafers). Cells exposed to Ga and

Ag—Ga exhibited round morphology with bright green fluorescence for cytoskeleton and clear nucleus similar to cells in the control group (Figure 5b), indicating healthy cell growth. The healthy sign of cells growing on Ag—Ga thin layer supported the finding that Ag—Ga suspension is cytocompatibility.

Cell migration is a process of cell movement from one area to another and is commonly used to access the wound healing.[53] In this study, the fibroblast (HFF) cells were cultured until they reached ≈80% confluence. The cell surfaces were then deliberately scratched using a wound maker (as indicated by black dotted lines in Figure 5c). The remaining surfaces were incubated in growth medium, and cell migration across the scratched area was monitored in real-time using imaging techniques (IncuCyte SX5 live-cell analysis system).

To investigate the potential of the Ag—Ga suspensions to promote cell proliferation and migration, the remaining cell sheets were exposed to Ag—Ga conditioned medium (DMEM with 10% FBS). Microscopy images showed that the cells proliferated and migrated across the scratched area after 24 h, with significant area coverage by 48 h. In comparison, the positive control cells, treated with DMEM and 10% FBS, exhibited rapid cell migration and completely covered the scratched area by 48 h. However, the cells treated with Ag-conditioned medium did not demonstrate any migration. These findings confirm that Ag—Ga suspension is compatible with cell proliferation and migration and has potential in biomedical applications.

2.5. Animal Studies

2.5.1. In Vivo Antibacterial Activity of Ag—Ga Surface-Coating Implants

In recent years, biodegradable magnesium (Mg) metal has been an emerging research topic.[54] The interest in this metal and its alloys stems from the fact that the elastic modulus of Mg is close to that of natural cortical bone.[55] Magnesium alloys are expected to be used as a bone-conductive and biodegradable orthopedic implants and to enter clinical practice.[56] However, Mg and its alloys do not provide protection against infection. In order to verify the applicability of the Ag—Ga particles, we coated them on Mg discs and evaluated their antibacterial activity in vivo (**Figure 6**a). For this experiment, we spray-coated Ga, Ag ion, and the Ag—Ga nano-amalgam suspension onto Mg discs. Next, the Mg (short for Mg discs), Ga@Mg (Ga coated group), Ag@Mg (Ag coated group), and Ag—Ga@Mg (Ag—Ga coated group) discs were implanted subcutaneously in the lateral skin of the right hindlimb of each Sprague Dawley (SD) rat. After bacterial recovery and concentration dilution, bacteria suspension with concentration ≈10^6 CFUmL^{-1} in 50 µL PBS of *S. aureus* or *E. coli* were injected directly onto the disc surface to establish a subcutaneous bacterial infection (Figure 6b). After 7 days, the rats were sacrificed, the implantation site was isolated and carefully opened to remove the discs. It was observed that some magnesium discs have been absorbed (Figure S10, Supporting Information). The internal surfaces were examined on day 7. As shown in Figure 6c, capsule formation surrounded the cavity where the implant was located. During the macroscopic examination of the bacteria-infected tissues, we observed the presence of obvious local abscesses specifically in the Mg group, and mild infections in the Ga@Mg and Ag@Mg groups, and the Ga@Mg group appeared to be more severe than the Ag@Mg group. Intriguingly, soft granulation tissue appeared after being implanted with Ag—Ga@Mg discs, and there was no abscess, which indicated an anti-inflammatory effect of the Ag—Ga coating (Figure 6c). Meanwhile, the changes in the blood test of the rats were monitored on the 14th day after surgery. A healthy trend of blood markers was measured for all groups, indicating that the inflammatory response was confined to the local area of infection and caused little alteration in the rats' general health (Figure 6d). To measure the toxicity of the surface coating, H&E staining was carried out on critical organs, including the heart, liver, spleen, lungs, and kidneys after a two-week period. As shown in Figure S11(Supporting Information), there was no detectable damage to these organs, indicating that the material is histologically safe. In addition, detecting the metal ion content in organisms for 3–12 months is an important method of testing subchronic toxicity. Due to the fact that subcutaneous implantation only lasted for 2 weeks, we did not conduct chronic toxicity testing for 3–12 months, which is also a limitation of this study. We will conduct subchronic toxicity testing in future long-term animal experiments.

In addition, the skin at the implantation site was cut off and used for histopathology. Slices from the soft tissues at the surgical sites after 7 days of bacterial infection were processed by H&E staining, Masson staining, and Giemsa staining to evaluate the inflammatory infiltration, morphological changes, and bacterial residues of collected tissues, respectively. As demonstrated in Figure 6e (subcutaneous *S. aureus* infection model) and Figure S12 (Supporting Information) (subcutaneous *E. coli* infection model), significant necrosis, abscesses, and destruction of muscular tissue with infiltration of inflammatory cells, indicative of a typical soft tissue infection, were observed in both the control and Ga coating groups, whereas ameliorated signs of bacterial infection were discovered in the Ag coating group, which was consistent with the findings presented in Figure 6c. On the contrary, the combination of the Ag—Ga coating group significantly improved the outcomes of subcutaneous bacterial infection compared to other groups. In addition, the Immunohistochemical results indicated that the expression of inflammatory markers COX-2, INOS, and macrophage marker CD68 decreased in the Ag—Ga group relative to the other groups (Figure 6f,g).

2.5.2. In Vivo Evaluation in an MRSA-Induced Rat Femoral Osteomyelitis Model

Osteomyelitis is an infection caused by microorganisms and accompanied by an inflammatory process and bone destruction.[57] The use of implants is a major risk factors for the occurrence of osteomyelitis. Because implants significantly elevate the risk of osteomyelitis, prioritizing the prevention and treatment of peri-prosthetic joint infection (PJI) is crucial for managing the condition.[58] The main pathogenic bacteria of osteomyelitis are *Staphylococcus aureus* and coagulase-negative staphylococci (CoNS) such as *Staphylococcus epidermidis* and *Staphylococcus lugdunensis*.[59] In orthopedics, antibiotic resistance remains a challenge during treatment of osteomyelitis. ≈50% of

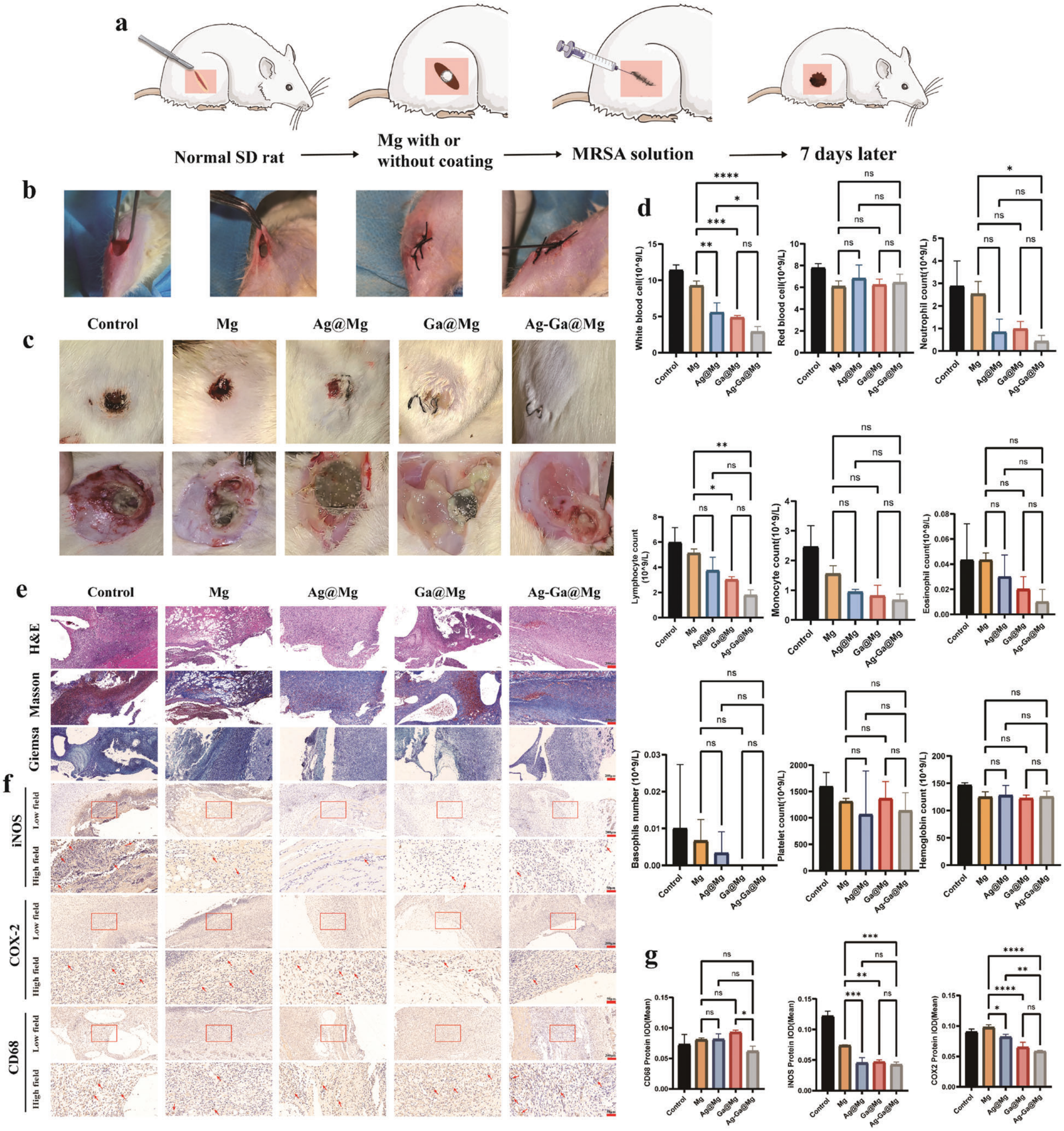

Figure 6. In vivo antibacterial activity of Ag─Ga surface-coating implants. a) Basic workflow of the animal experiments. b) Intraoperative process of model building. c) Representative images of external and internal surfaces of skin where the implant was located. d) The changes in the ordinary blood test. e) Representative images of H&E staining, Masson staining, and Giemsa staining of skin surrounded the implants in subcutaneous *S. aureus* infection model. Scale bars, 200 µm. f) The Immunohistochemical results of inflammatory markers COX-2, INOS, and macrophage marker CD68. Scale bars, 200 µm (low field), 50 µm (high field). g) Statistical analysis for IOD of COX-2, INOS, and CD68 based on immunostaining result. Error bar represents mean ± s.d.; $n = 3$, $^{***}p < 0.001$, $^{**}p < 0.01$, $^{*}p < 0.05$.

implant-related infections are caused by *Staphylococcus aureus*,[60] especially MRSA.

The excellent biocompatibility of Ag─Ga coating prompted us to establish a MRSA-induced rat femoral osteomyelitis model in male Sprague Dawley rats using a traditional Titanium rod to assess the antibacterial efficacy and bone regeneration ability of the material in vivo (**Figure 7**a; Video S1, Supporting Information). After injecting MRSA bacterial suspension into the femoral marrow cavity of rats for 2 weeks, signs of cortical bone destruction, osteolysis, and periosteal reaction were observed in the rats' femurs, indicating the onset of osteomyelitis (Figure 7b), and the X-ray results of the femurs of different groups of rats are shown

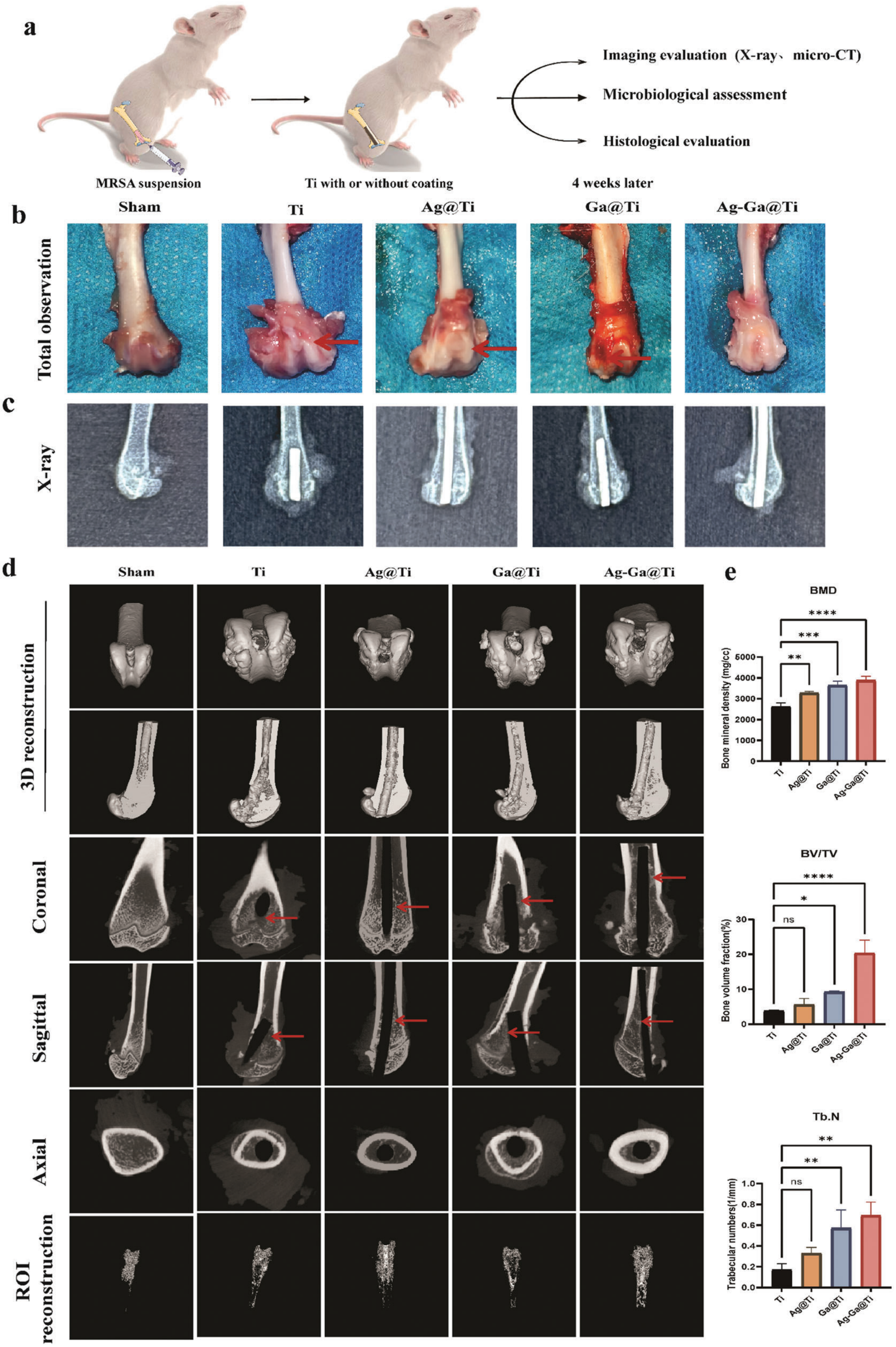

Figure 7. In vivo anti-infective assessment in an MRSA-induced rat femoral osteomyelitis model. a) Schematic illustration of the MRSA-injected femoral osteomyelitis model. b) Gross investigations of rat femurs at specified times. c) Representative X-ray images. d) Representative images of Micro-CT images. e) Quantitative results of bone mineral density (BMD), bone volume fraction (BV/TV) and trabecular number (Tb.N) in the ROI. Error bar represents mean ± s.d.; $n = 3$, $^{***}p < 0.001$, $^{**}p < 0.01$, $^{*}p < 0.05$.

in Figure 7c. X-ray evaluation showed that the Ti group of rats showed obvious signs of osteolysis and periosteal reaction. However, very few signs of osteolysis were observed in the Ag—Ga@Ti group (Figure 7c). Femurs were collected from rats at 14 days postoperatively and examined for osteolysis and tissue regeneration via micro-CT (Figure 7d). Micro-CT results revealed the presence of MRSA-induced cavitation in the femoral structures of the Ti, Ag@Ti, and Ga@Ti groups at 14 days after surgery. However, the Ag—Ga@Ti group exhibited superior bone repair compared to the other groups. Interestingly, the bone mineral density (BMD), the bone volume to total volume (BT/TV), trabecular number (Tb.N.), and trabecular thickness (Tb.Th) were much higher for the group treated with Ag—Ga@ Ti than for the other three groups, while the trabecular separation (Tb.Sp) was the lowest, implying the superior antimicrobial effect and osteogenic properties of Ag—Ga coating (Figure 7e; Figure S13, Supporting Information).

H&E staining was performed to detect the degree of inflammation in the bone tissue surrounding the implants (**Figure 8**a). After a 2-week treatment period, the Ti and Ga@Ti groups exhibited a significant presence of inflammatory cells, including lymphocytes and neutrophils. In contrast, the Ag@Ti and Ag—Ga@Ti groups showed minimal infiltration of inflammatory cells. These observations were consistent with the results obtained by the Giemsa staining (Figure 8b). Additionally, Masson staining revealed a notable reduction in the inflammatory response and increased collagen deposition in the bone tissues treated with Ag—Ga@Ti (Figure 8c). To further investigate the immune microenvironment of infected bone tissue, we performed immunohistochemical staining of inflammatory markers. Notably, the Ag—Ga@Ti group exhibited the lowest expression levels of iNOS (Figure 8d,e), and COX-2 (Figure 8f,g), which are widely recognized biomarkers of inflammation.[61] This indicates a decrease in the inflammatory response within the Ag—Ga@Ti-treated tissues. By providing these comprehensive findings, we contribute to a better understanding of the anti-inflammatory effects of the Ag—Ga coating. These results highlight the potential of this new material as a promising treatment option for reducing inflammation in infected bone tissue.

To further investigate the ability of the Ag—Ga coating to promote bone regeneration, we conducted immunohistochemical staining of the femur to examine indicators associated with osteogenesis. The results, presented in Figure 8h,k, demonstrated a higher expression of Collagen I and TGF-β1 in the Ag—Ga@ Ti group, providing compelling evidence for the excellent osteogenic performance of the Ag—Ga coating. These findings support the notion that the Ag—Ga coating possesses desirable antibacterial and osteogenic properties, particularly in the context of deep tissue infections. Furthermore, the coating showed potential in countering MRSA, thereby reducing bone tissue erosion and facilitating bone tissue regeneration. Notably, its effectiveness in transparent cartilage regeneration was also noteworthy.

2.5.3. In Vivo Promotion of Osteogenic Ability in Rat Critical-Size Calvarial Defect Model

The implantation of a process that is particularly vital for addressing larger bone defects, is vital for the biomaterial to facilitate bone regeneration. In this experiment, a critical-size rat skull defect model was used to assess the effectiveness of Ag—Ga coating-induced bone healing (**Figure 9**a).[62] Briefly, a skull defect with a diameter of 8 mm was generated in the parietal bone using a drill. The defect was centered around the sagittal suture line, specifically between lambda and the anterior chamber. Then the Mg discs sprayed with Ga, the Ag ion, and the Ag—Ga nano-amalgam suspensions were carefully inserted into the bone defect (Figure 9b). After 8 weeks, the recovery of skull defects in the different rat groups was evaluated by Micro-CT analysis. Figure 9c displayed the 3D reconstruction of Micro-CT images of rat skull defects at the 8-week mark. Notably, there were significant differences among the four groups: Micro-CT images of the bone defect showed that Ag—Ga coating significantly accelerated the formation of new bones after 6 weeks. The range of bone defects in the pure Mg discs decreased compared to the control group, but there is still a significant difference compared to the Ag—Ga coating group.

Then, histological analysis was conducted to analyze the tissue in the area of the skull defect. At 8 weeks after surgery, significant differences in differentiation were observed in the sagittal plane of the skull defect, as shown in Figure 9d. H&E staining revealed an increased amount of generated tissue in the Ag—Ga@Mg group compared to the other three groups (Figure 9d). Furthermore, Masson's trichrome staining demonstrated a substantial formation of bone-like matrix and collagen in the scaffold treated with Ag—Ga@Mg discs, while the other groups only showed a small number of collagen fibers (Figure 9e), which is consistent with the Micro-CT results. Additionally, immunohistochemical staining was performed on BMP-2, BMPR, and Runx-2 to further evaluate the effectiveness of Ag—Ga coating on bone regeneration. Immunohistochemical staining revealed a larger area of BMP-2, BMPR, and Runx-2 positive cells in the Ag—Ga@Mg group compared to the other three groups (Figure 9f). Moreover, the expression of BMP-2, BMPR, and Runx-2 was quantitatively analyzed using ImageJ software. Statistical analysis indicated that the Ag—Ga@Mg group exhibited significantly higher expression levels of osteogenic factors compared to the Ga@Mg and Ag@Mg groups, which means the Ag—Ga coating significantly accelerated the formation of new bones (Figure 9g).

3. Conclusion

In summary, we developed a simple and controllable method for synthesizing Ag—Ga nano-amalgamated particles in the form of a suspension, which can be spray-coated onto a variety of material surfaces to impart antibacterial properties. The method employs gallium liquid metal to reduce Ag ions in an aqueous solution ($AgNO_3$) through galvanic replacement. The critical role of gallium liquid metal (GaLM) in the Ag—Ga nano-amalgamated particles is multifaceted and pivotal. GaLM not only serves as a carrier for silver nanocrystals through the galvanic replacement process, but also facilitates a controlled, slow-release mechanism for silver ions, which attenuates the pronounced toxicity associated with high concentrations of Ag ions. The Ag—Ga nano-amalgam suspension displayed remarkable potential in creating surfaces that combat prevalent pathogenic bacteria, such as *P. aeruginosa* and *S. aureus*, achieving an efficacy nearly equivalent to that of silver ions at similar concentrations. Interestingly, GaLM

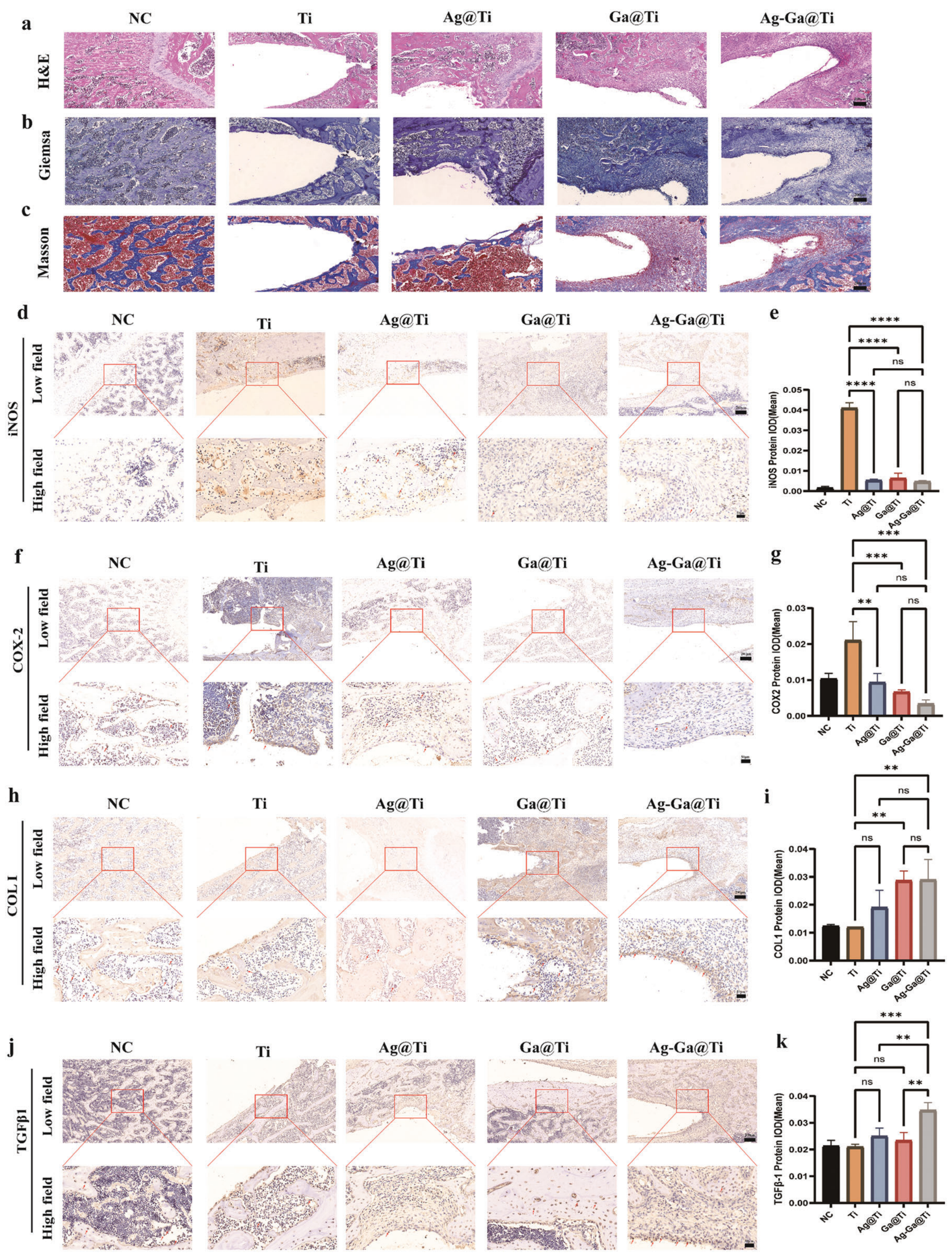

Figure 8. Histological assay of MRSA-induced rat femoral osteomyelitis model. a–c) Representative photos of H&E staining, Giemsa staining, and Masson staining to evaluate the inflammatory infiltration. Scale bars, 200 µm. d) Representative images of Immunohistochemical staining of iNOS in different indicated groups. Scale bars, 200 µm (low field), 50 µm (high field). e) Statistical analysis for IOD of INOS based on immunostaining results. f,g) Immunohistochemical staining of COX-2. Scale bars, 200 µm (low field), 50 µm (high field). h) COL-1 immunohistochemical staining of the representative implant was performed on different groups. Scale bars, 200 µm (low field), 50 µm (high field). i) Statistical analysis for IOD of COL-1 based on immunostaining result. j,k) Immunohistochemical staining of TGF-β1. Scale bars, 200 µm (low field), 50 µm (high field). Scale bars, 200 µm (low field), 50 µm (high field). Error bar represents mean ± s.d.; $n = 3$, $^{***}p < 0.001$, $^{**}p < 0.01$, $^{*}p < 0.05$.

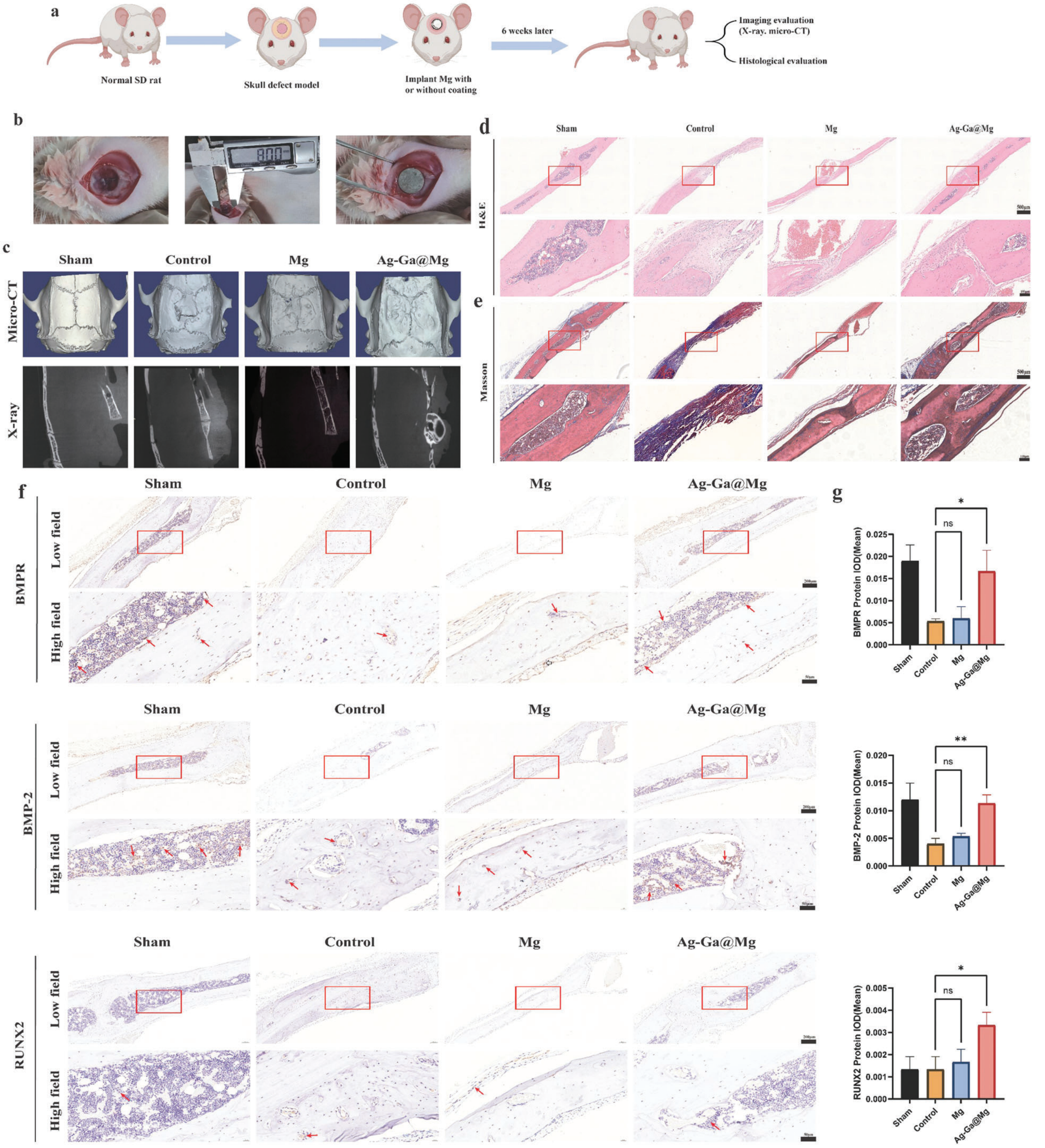

Figure 9. In vivo promoting osteogenic ability in rat critical-size calvarial defect model. a) Schematic illustration of calvarial defect establishment treatment modalities. b) Intraoperative process of model building. c) Representative 3D reconstruction of Micro-CT images. d) Representative images of H&E staining, and e) Masson staining Scale bars, 500 µm (low field), 100 µm (high field). f) The Immunohistochemical staining of BMP-2, BMPR, and Runx-2 positive cells in different groups. g) Statistical analysis for IOD of BMP-2, BMPR, and Runx-2 based on immunostaining results. Error bar represents mean ± s.d.; $n = 3$, $^{***}p < 0.001$, $^{**}p < 0.01$, $^{*}p < 0.05$.

mitigates the pronounced toxicity of Ag^+, resulting in an Ag—Ga amalgam that is biocompatible with human fibroblast and keratinocyte cells. In contrast, these cells displayed a significant decrease in viability when exposed to Ag-only coated surfaces. In vivo studies using a rat model further highlight the antibacterial potency of the Ag—Ga coatings, specifically against methicillin-resistant *S. aureus* and *E. coli*, when placed on implants such as titanium rods and magnesium discs. Moreover, the outcomes of the histological analyses conducted on rat models indicated that implants coated with Silver—gallium demonstrated histologically to be non-toxic to tissue. Evaluations of the animal internal organs revealed that normal functionality was maintained for two weeks subsequent to the transplantation procedure. Additionally, the Ag—Ga coating was associated with a prominent formation of bone-like matrix and collagen scaffolding without eliciting an inflammatory response. As detailed in this study, the attributes of the Ag—Ga underscore the potential of this new material as a prime candidate for generating antimicrobial and biocompatible coatings, making them suitable for preventing infections with a range of medical materials and devices.

4. Experiment section

Preparation of Ag—Ga Suspension: A solid gallium piece (≈57 mg) was added to 10 mL of water and sonicated for different times from 15 to 35 min in a standard probe sonication (Vibra-Cell, Sonics) with an ice bath to form the Ga particles suspension. Pluronic F-127 (Sigma—Aldrich) was dissolved in water to make 10% solution and silver nitrate (Sigma—Aldrich) was dissolved in water to make solution at concentration of 10 mg ml^{-1}. The different concentrations of Ag—Ga nanoamalgamated particles solution was made up by adding concentrated silver nitrated solution into Ga particles, and then mixing using a vortex mixer before the addition of F-127 (Figure 1a) in the ratio silver atomic percentage of 0, 1.5, 3.0, 4.0, and 6.0% respectively. To prepare thin films for testing, an aliquot of 20, 40, 80, and 160 μL of each sample were pipetted into wells of 96 well-plates and dried at room temperature. These thin films were used for antimicrobial and viability tests.

Scanning Electron Microscopy (SEM) Characterization: The surface morphology and chemical composition of Ag—Ga synthesis were examined using SEM (FEI Inspect F50). The synthesized suspensions were imaged at 3 kV and the images were analyzed using ImageJ software. The chemical composition of Ag—Ga representing in scanning region and underlying of the suspension was examined by EDS spectra. For bacteria cellular imaging, Ag—Ga and Ga suspensions were deposited on silicon wafers. *P. aeruginosa* and *S. aureus* cultures (OD ≈ 0.1) were then placed on silicon wafers coated with Ga, Ag, and Ag—Ga, then incubated at 37 °C for 18 h. Bacterial cells were also incubated on the silicon wafer to serve as control. After incubation period, the bacterial cells were fixed with glutaraldehyde in 0.1 M sodium cacodylate buffer pH 7.4, 4% (ProSciTech, Australia) for 45 min. The cells were then dehydrated with a graded ethanol series (30, 50, 70, 80, 90, 95, and 100%) in 10 min for each concentration. Before imaging, the samples were air-dried and coated with a thin platinum film using an Ion Sputter Coater (TB-SPUTTER, Quorum Technologies, UK).

X-Ray Photoelectron Spectroscopy Characterization: Surface chemistry was assessed via X-ray photoelectron spectroscopy (XPS), obtaining spectra for Ag 3*d*, Ga 2*d*, C 1*s*, and O 1*s*. A Thermo Scientific K-alpha XPS spectrometer with an Al K*α* X-ray source (1486.7 eV) and a surrounding hemispherical electron analyzer were utilized. Samples of Ga, Ag—Ga, and Ag were set on silicon bases. The acquired XPS data were processed using the CasaXPS software, referencing the C 1*s* peak at 285 eV for charge.[63]

Transmission Electron Microscopy (TEM) Characterization: A JEOL JEM-2100F transmission electron microscope (TEM) was operated at an acceleration voltage of 200 kV to capture low- and high-resolution TEM images of the samples. The TEM samples were prepared by depositing dilute solutions of Ga and Ag—Ga suspensions onto TEM grids. The TEM images were obtained and analyzed using the Gatan Digital Micrograph software package.

X-Ray Crystallography (XRD): After producing Ga and Ag—Ga droplets, samples were washed with water, and drop-casted onto glass slides and allowed to dry.[64] XRD patterns were taken with a Bruker D4 diffractometer utilizing Cu K*α* radiation (1.5418 Å). The collected data was then processed to create line charts using the Origin 2023 software.

Inductively Coupled Plasma Mass Spectrometry (ICP-MS): To evaluate the release of Ga and Ag ions from the Ga-F127, Ag—Ga-F127, and Ag-F127 samples, these were submerged in 0.5 mL of TSB media maintained at 37 °C over 24 h. Once the incubation period finished, the supernatants were collected and filtered to ensure any impurities or granules were removed. This liquid underwent treatment with HNO_3 to break down any residual solids and was subsequently diluted to keep the concentration <5%, this is to minimize complications during ICP-MS evaluations. The Varian 720-ES system, America, was employed to measure Ga and Ag ion content in the liquid using ICP-MS. Calibration of this device was done using reference solutions of specified concentrations. The ion content in the original samples was ascertained using a comparison curve derived from these reference solutions.

Bacteria Strains and Culture: The bacterial strains, specifically *Staphylococcus aureus* ATCC 25923 and *Pseudomonas aeruginosa* ATCC 15692, were maintained at −80 °C. To initiate the experiments, the acquired bacterial strains were streaked on tryptic soy agar (TSA, Oxoid) plates. A single colony was selected from each plate, suspended in 10 mL of sterilized Tryptic Soy Broth (TSB, Oxoid), and incubated at 37 °C with shaking for 18 h before being used for the experiments.

Antibacterial Studies: The antibacterial activity of Ag—Ga suspension was assessed against *S. aureus* and *P. aeruginosa* using CFU counting method. Briefly, 100 μL of bacteria cultures (10^6 CFU mL^{-1}), *S. aureus* and *P. aeruginosa*, were added to 96-well plate containing samples as prepared in Section 2.2 and incubated for 24 h at 37 °C. After incubation period, serial dilution of 1:10, 1:100, and 1:1000 (v/v) were prepared from the overnight cultures and 5 μL of each dilution was spread onto tryptic soy agar (TSA) plates. The plates were incubated for 18 h at 37 °C and the number of colonies was counted. Log reduction was calculated and compared to control samples (untreated bacteria). The experiment was conducted in triplicate.

Well Diffusion Assay: Bacteria cultures (10^6 CFU mL^{-1}) were spread on TSA plates. Wells (5 mm) were cut into the agar plates with sterilized cork borer and then 50 μL of Ag—Ga suspension was pipetted into the wells. $AgNO_3$, Ga, and AgNPs solutions (50 μL) were also poured into each well for antibacterial property comparison. Inoculated plates were then incubated at 37 °C for 24 h for zone inhibition.

Live and Dead Staining: After incubation of bacterial on the silicon wafers coated Ag, Ag—Ga, and Ga, samples were rinsed twice with (PBS) and then stained with the LIVE/DEAD BacLightTM Viability Kit (containing SYTO9 and propidium iodide, PI) at room temperature for 10 min in the dark. The samples were observed using a ZEISS LSM 880 microscope (Zeiss, Germany). All experiments were performed in triplicate.

Membrane Potential Staining: Following the incubation of bacteria on silicon wafers coated with Ag, Ag—Ga, and Ga, each sample was subjected to two washes with Phosphate-Buffered Saline (PBS). The samples were then stained with 1 μM of 2′,7′-dichlorodihydrofluorescein diacetate (H_2DCFDA), supplied by Invitrogen, Australia, and left at room temperature for 10 min in a dark setting. Following another wash with PBS, these samples were analyzed using a ZEISS LSM 880 microscope, manufactured by Zeiss, Germany.

Reactive Oxygen Species Staining: Post-incubation of bacteria on silicon wafers that had been coated, the samples underwent two washes with Phosphate-Buffered Saline (PBS). Following this, samples were treated with 1 μM of DiO stain from Biotium Corp., Hayward, CA, USA, and left to sit in darkness for 5 min. Subsequently, 2 μM of DPA was introduced to the bacterial mixture and allowed to incubate for another 45 min in a dark environment. Finally, fluorescence imagery was acquired using Confocal Laser Scanning Microscopy (CLSM).

Synchrotron ATR-FTIR Operation and Data Analysis: The spatial distribution of chemical functional groups in both untreated and treated bacteria with Ag—Ga, Ga, and Ag was studied using ATR-FTIR mapping. This research took place at the Infrared Micro-spectroscopy beamline of the Australian Synchrotron, utilizing a Bruker Hyperion 3000 FTIR microscope linked to a VERTEX V80v FTIR spectrometer from Bruker Optik GmbH in Ettlingen, Germany. This used a distinct macro ATR-FTIR equipment which included a 250 μm diameter germanium (Ge) ATR crystal (with a refractive index of $n_{Ge} = 4.0$) and a 20 × IR objective (with a numerical aperture of NA = 0.60).66 Pathogen bacteria was exposed to Ag—Ga, Ga, and Ag for a duration of 3 h at a temperature of 37 °C. After air-drying, both the untreated and treated samples were positioned on aluminum discs, which were then placed on the macro ATR-FTIR instrument's sample stage. Using the OPUS 8.0 software from Bruker, spectral parameters such as a range between 3900 and 950 cm^{-1} and a resolution of 4 cm^{-1} was set. This software also allowed to create chemical maps by calculating the area under specific peaks in the spectral data. For in-depth multivariate data analysis, this utilized CytoSpec v. 1.4.02 from Cytospec Inc. in Boston, MA, USA, and the UnscramblerX 11.1 software by CAMO Software AS, located in Oslo, Norway. The data analysis process will be presented in Text S1 (Supporting Information).

Mammalian Cell Culture: human epidermal keratinocyte cells (HaCaT, 300493, cell line services, Eppelheim, Germany) and human fibroblast cells (HFF-1 SCRC-1041, USA) were used in this study. The cells were stored in liquid nitrogen until reviving using the ATCC standard protocol. Briefly, 1 mL of frozen cells were thawed in a 37 °C water bath and then diluted with 5 mL of fresh Dulbecco's modified Eagle's medium (DMEM) (for adherent cell) supplemented with 10% fetal bovine serum (FBS) and 1% penicillin/streptomycin (Gibco, Thermo Fisher Scientific). The mixture was centrifuged at 200 rcf for 5 min and the pellet was resuspended in fresh media and incubated in humidified air atmosphere containing 5% CO_2 at 37 °C in either T25 or T75 flasks (Corning, NY). The media was changed every 2 to 3 days, and the cells were sub-cultured when they reached the confluency ≈80%. The HaCaT cells were detached from the flask, using 0.25% Trypsin-EDTA (Gibco, Thermo Fisher Scientific) before conducting any experiments. Cell number and viability were determined using a trypan blue exclusion test with an automated Countess III Cell Counter (Thermo Fisher Scientific). Before conducting any experiments, the cells were grown for at least 1 week after thawing to ensure stability and viability.

Cell Viability Assay: Cell viability was assessed via a cell counting kit-8 (CCK8) assay (Ab228554, Abcam, Australia). Briefly, 100 µL of cells in media were added to 96-well plate containing samples as prepared in section of preparation of Ag—Ga suspension and incubated at 37 °C with 5% (v/v) CO_2 atmosphere. The untreated wells with cells seeding were used as positive control for viability. Cells were seeded into the plates with a density of 1×10^5 cells per well. After 24 h of incubation, 10% of CCK8 solution was added to each well and the cells were incubated for 4 h. The absorbances were measured at 460 nm using a BioTek Synergy HTX Multimode microplate reader. All assays were studied in triplicate.

Immunofluorescence Staining: Cells were fixed with 4% paraformaldehyde in phosphate-buffered saline (PBS) (Sigma–Aldrich) for 20 min. Following fixation, cells were rinsed using PBS and then treated with a 0.1% Triton-X solution in PBS for 3 to 5 min, after which they were again washed with PBS. Subsequently, the cells were exposed to a mixture of DAPI and phalloidin (both from Invitrogen, Life Technologies) in PBS and allowed to sit for 30 min at room temperature. Excess dye was then removed by another PBS wash. Finally, cell imaging was carried out using an Olympus IX83 fluorescence microscope, with excitation wavelengths of 365 and 489 nm, respectively.

Cell Migration Assay: The IncuCyte SX5 live-cell analysis system (Sartorius) was utilized for the real-time scratch closure experiment. The human fibroblast (HFF) cells were seeded on 96-well plates at a density of 1×10^5 cells per well and incubated at 37 °C with 5% CO_2 for 24 h to allow cell attachment and growth. Scratch was created by consistently scraping the cells in each well using a wound maker. The detached cells were then removed by washing with PBS solution, and fresh growth medium (DMEM/F12 + containing 10% FBS, 100 units mL^{-1} penicillin, and 100 µg mL^{-1} streptomycin) was added to the control wells. In the test wells, 100 µL of growth medium containing 10% of Ag—Ga or Ag suspension were added. The plates were incubated in the IncuCyte SX5 system for 48 h at 37 °C with 5% CO_2 and 95% humidity. Images were captured after 24 h and 48 h (period until the scratch wound was completely closed).[65] The width of the scratch was subsequently measured after 0, 24, and 48 h using ImageJ software.

Animal Experiment: The authors purchased 10-week-old male Sprague Dawley rats from Beijing Vital River Laboratory Animal Technology Co., Ltd. The rats were housed under controlled identical specific pathogen-free standard environmental conditions (23 ± 2 °C, 12 h light/dark cycle) with free access to food and allowed to move freely. All animal treatments and surgical procedures were conducted in accordance with the guidelines of the Ethics Committee on Animal Experiments of Shandong University in China (Approval No. 23027). The process of performing tests on rats and data analysis are detailed in Text S2 (Supporting Information).

Statistical Analysis: All experiments were repeated twice with at least three replications. The results are expressed as the mean ± SD, and GraphPad Prism 7.0 (GraphPad Software, Inc., USA) was used for the analysis. One-way ANOVA was used to determine statistical significance. Differences were considered significant at $p < 0.05$.

Supporting Information

Supporting Information is available from the Wiley Online Library or from the author.

Acknowledgements

T.T.N., P.Z. and J.B. contributed equally to this work. K.V. thanks NHMRC for the Fellowship GNT1194466 and ARC for grant DP220103543. V.K.T. acknowledges the support from the Flinders Foundation Health Seed Grant. This work was supported by the National Natural Science Foundation of China (Grant No. 82072478 to Yunpeng Zhao), the Shandong Provincial Natural Science Foundation (Grant No. ZR2020YQ54, to Yunpeng Zhao), The Jinan clinical medicine and technological innovation plan (grant No. 202019195 to Hao Wang) and Shandong First Medical University Youth Science Foundation Incubation Project (grant no. 202201-063 to Hao Wang). The authors acknowledge the facilities, and the scientific and technical assistance of Microscopy Australia and the Australian National Fabrication Facility (ANFF) under the National Collaborative Research Infrastructure Strategy, at the South Australian Regional Facility, Flinders Microscopy and Microanalysis, Flinders University. The authors would also like to thank the RMIT Microscopy and Microanalysis Facility (RMMF). This research was undertaken on the IR microspectroscopy beamline at the Australian Synchrotron, part of ANSTO. The animal experiments were approved by the institutional review board of Shandong University. The authors would like to acknowledge the Translational Medicine Core Facility of Shandong University for consultation and instrument availability that supported this work.

Open access publishing facilitated by Flinders University, as part of the Wiley - Flinders University agreement via the Council of Australian University Librarians.

Conflict of Interest

The authors declare no conflict of interest.

Data Availability Statement

The data that support the findings of this study are available from the corresponding author upon reasonable request.

Keywords

antibacterial, biocompatibility, gallium, liquid metal, silver

Received: August 6, 2023
Revised: October 10, 2023
Published online:

[1] a) C. R. Arciola, D. Campoccia, L. Montanaro, *Nat. Rev. Microbiol.* **2018**, *16*, 397; b) R. Jamaledin, C. K. Y. Yiu, E. N. Zare, L.-N. Niu, R.

Vecchione, G. Chen, Z. Gu, F. R. Tay, P. Makvandi, *Adv. Mater.* **2020**, *32*, 2002129; c) P. Singha, J. Locklin, H. Handa, *Acta Biomater.* **2017**, *50*, 20; d) M. Vallet-Regí, D. Lozano, B. González, I. Izquierdo-Barba, *Adv. Healthcare Mater.* **2020**, *9*, 2000310.

[2] Z. Saleem, B. Godman, M. A. Hassali, F. K. Hashmi, F. Azhar, I. U. Rehman, *Pathog. Glob. Health* **2019**, *113*, 191.

[3] B. Allegranzi, S. B. Nejad, C. Combescure, W. Graafmans, H. Attar, L. Donaldson, D. Pittet, *Lancet* **2011**, *377*, 228.

[4] S. B. Goodman, Z. Yao, M. Keeney, F. Yang, *Biomaterials* **2013**, *34*, 3174.

[5] Z. P. Sinagra, J. S. Davis, M. Lorimer, R. N. De Steiger, S. E. Graves, P. Yates, L. Manning, *Bone Jt. Open* **2022**, *3*, 367.

[6] K. Vickery, H. Hu, A. S. Jacombs, D. A. Bradshaw, A. K. Deva, *Healthcare Infect.* **2013**, *18*, 61.

[7] M. Wang, T. Tang, *J. Orthop. Translat.* **2019**, *17*, 42.

[8] H. Chouirfa, H. Bouloussa, V. Migonney, C. Falentin-Daudré, *Acta Biomater.* **2019**, *83*, 37.

[9] a) T.-F. Mah, B. Pitts, B. Pellock, G. C. Walker, P. S. Stewart, G. A. O'Toole, *Nature* **2003**, *426*, 306; b) K. Yu, J. C. Y. Lo, M. Yan, X. Yang, D. E. Brooks, R. E. W. Hancock, D. Lange, J. N. Kizhakkedathu, *Biomaterials* **2017**, *116*, 69.

[10] Smith-Nephew, Acticoat-Antimicrobial Barrier Dressing, https://smith-nephew.com/en-us/health-care-professionals/products/advanced-wound-management/acticoat-global, (accessed: May, 2023).

[11] 3M Tegaderm Transparent Film Dressing, https://www.3m.com.au/3M/en_AU/p/d/v000180349/, (accessed: May, 2023).

[12] KCI, V.A.C. GRANUFOAM SILVER Dressing Kits, https://www.acelity.com/healthcare-professionals/global-product-catalog/catalog/vac-granufoam-silver-dressing-kits, (accessed: May, 2023).

[13] A. BrightSky, Bardex IC Silver Coated Cath 30 ml 43 cm M FG20, https://brightsky.com.au/product/bardex-ic-silver-coated-cath-30ml-43cm-m-fg20/, (accessed: May, 2023).

[14] Medtronic, PALINDROME PRECISION CHRONIC HEMODIALYSIS CATHETERS, https://www.medtronic.com/covidien/en-us/products/dialysis-access/chronic-vascular/palindrome-catheters.html, (accessed: May, 2023).

[15] Teleflex, Arrowg+ard Blue Plus CVC, https://www.teleflex.com/usa/en/product-areas/vascular-access/central-access/short-term-cvc/index.html, (accessed: May, 2023).

[16] a) M. Fiore, A. Sambri, R. Zucchini, C. Giannini, D. M. Donati, M. De Paolis, *Eur. J. Orthop. Surg. Traumatol.* **2021**, *31*, 201; b) J. Hardes, M. P. Henrichs, G. Hauschild, M. Nottrott, W. Guder, A. Streibuerger, *The J. of Arthroplasty* **2017**, *32*, 2208; c) M. C. Parry, M. K. Laitinen, J. I. Albergo, C. L. Gaston, J. D. Stevenson, R. J. Grimer, L. M. Jeys, *Eur. J. of Surgical Oncology* **2019**, *45*, 704.

[17] a) I. X. Yin, I. S. Zhao, M. L. Mei, Q. Li, C. H. Chu, *Int J Nanomedicine* **2020**, *15*, 2555; b) S. Anees Ahmad, S. Sachi Das, A. Khatoon, M. Tahir Ansari, M. Afzal, M. Saquib Hasnain, A. Kumar Nayak, *Materials Science for Energy Technologies* **2008**, *3*, 756.

[18] a) M. Rai, A. Yadav, A. Gade, *Biotechnol. Adv.* **2009**, *27*, 76; b) M. E. Stryjewski, H. F. Chambers, *Clinical Infectious Diseases* **2008**, *46*, S368.

[19] a) Y. Tao, T. Aparicio, M. Li, K. W. Leong, S. Zha, J. Gautier, *Nucleic Acids Res.* **2021**, *49*, 5074; b) T. C. Dakal, A. Kumar, R. S. Majumdar, V. Yadav, *Front. Microbiol.* **2016**, 7, 1831.

[20] a) G. Zhu, G. Wang, J. J. Li, *Mater. Adv.* **2021**, *2*, 6901; b) S. Bohara, J. Suthakorn, *Biomater. Res.* **2022**, *26*, 26; c) J. H. Sung, J. H. Ji, J. D. Park, J. U. Yoon, D. S. Kim, K. S. Jeon, M. Y. Song, J. Jeong, B. S. Han, Y. H. Chung, H. K. Chang, J. H. Lee, M. H. Cho, B. J. Kelman, I. J. Yu, *Toxicol Sci.* **2009**, *108*, 452.

[21] a) A. Panáček, L. Kvítek, M. Smékalová, R. Vecerová, M. Kolář, M. Röderová, F. Dycka, M. Sebela, R. Prucek, O. Tomanec, R. Zboril, *Nat. Nanotechnol.* **2018**, *13*, 65; b) A. Kędziora, M. Wernecki, K. Korzekwa, M. Speruda, Y. Gerasymchuk, A. Łukowiak, G. Bugla-Płoskońska, *Int. J. Nanomed.* **2020**, *15*, 199.

[22] X. Cheng, W. Zhang, Y. Ji, J. Meng, H. Guo, J. Liu, X. Wu, H. Xu, *RSC Adv.* **2013**, *3*, 2296.

[23] L. Xu, Y.-Y. Wang, J. Huang, C.-Y. Chen, Z.-X. Wang, H. Xie, *Theranostics* **2020**, *10*, 8996.

[24] P. V. Asharani, G. Low Kah Mun, M. P. Hande, S. Valiyaveettil, *ACS Nano* **2009**, *3*, 279.

[25] W. H. De Jong, L. T. M. Van Der Ven, A. Sleijffers, M. V. D. Z. Park, E. H. J. M. Jansen, H. Van Loveren, R. J. Vandebriel, *Biomaterials* **2013**, *34*, 8333.

[26] O. Mcneilly, R. Mann, M. Hamidian, C. Gunawan, *Front Microbiol.* **2021**, *12*, 652863.

[27] L. M. Stabryla, K. A. Johnston, N. A. Diemler, V S. Cooper, *Nature Nanotechnology.* **2021**, *16*, 996.

[28] A. Kędziora, R. Wieczorek, M. Speruda, I. Matolínová, T. M. Goszczyński, I. Litwin, V. Matolín, G. Bugla-Płoskońska, *Front Microbiol.* **2021**, *12*, 659614.

[29] a) S. Cheeseman, S. J. Bryant, L. Z. Y. Huang, E. L. H. Mayes, R. J. Crawford, T. Daeneke, J. Chapman, V. K. Truong, A. Elbourne, *ACS Appl. Nano Mater.* **2022**, *5*, 16584; b) D. Q. Pham, S. Gangadoo, C. C. Berndt, J. Chapman, J. Zhai, K. Vasilev, V. K. Truong, A. S. Ang, *ACS Appl. Mater. Interfaces* **2022**, *14*, 18974; c) J. Yang, P. Nithyanandam, S. Kanetkar, K. Y. Kwon, J. Ma, S. Im, J.-H. Oh, M. Shamsi, M. Wilkins, M. Daniele, T.-I. Kim, H. N. Nguyen, V. K. Truong, M. D. Dickey, *Adv. Mater. Technol.* **2023**, *8*, 2202183; d) S. Houshyar, A. Rifai, R. Zizhou, C. Dekiwadia, M. A. Booth, S. John, K. Fox, V. K. Truong, *J. Biomed. Mater. Res., Part B* **2022**, *110*, 1131; e) K. Y. Kwon, S. Cheeseman, A. Frias-De-Diego, H. Hong, J. Yang, W. Jung, H. Yin, B. J. Murdoch, F. Scholle, N. Crook, E. Crisci, M. D. Dickey, V. K. Truong, T.-I. Kim, *Adv. Mater.* **2021**, *33*, 2104298; f) V. K. Truong, A. Hayles, R. Bright, T. Q. Luu, M. D. Dickey, K. Kalantar-Zadeh, K. Vasilev, *ACS Nano* **2023**, *17*, 14406.

[30] a) F. Li, F. Liu, K. Huang, S. Yang, *Front. Bioeng. Biotechnol.* **2022**, *10*, 827960; b) C. H. Goss, Y. Kaneko, L. Khuu, G. D. Anderson, S. Ravishankar, M. L. Aitken, N. Lechtzin, G. Zhou, D. M. Czyz, K. Mclean, O. Olakanmi, H. A. Shuman, M. Teresi, E. Wilhelm, E. Caldwell, S. J. Salipante, D. B. Hornick, R. J. Siehnel, L. Becker, B. E. Britigan, P. K. Singh, *Sci. Transl. Med.* **2018**, *10*, eaat7520.

[31] C. Zhang, B. Yang, J. M. Biazik, R. F. Webster, W. Xie, J. Tang, F.-M. Allioux, R. Abbasi, M. Mousavi, E. M. Goldys, K. A. Kilian, R. Chandrawati, D. Esrafilzadeh, K. Kalantar-Zadeh, *ACS Nano* **2022**, *16*, 8891.

[32] F. Kurtuldu, N. Mutlu, A. R. Boccaccini, D. Galusek, *Bioact. Mater.* **2022**, *17*, 125.

[33] a) Y. Lin, Y. Liu, J. Genzer, M. D. Dickey, *Chem. Sci.* **2017**, *8*, 3832; b) Y. Lin, J. Genzer, W. Li, R. Qiao, M. D. Dickey, S.-Y. Tang, *Nanoscale* **2018**, *10*, 19871.

[34] a) T. Daeneke, K. Khoshmanesh, N. Mahmood, I. A. De Castro, D. Esrafilzadeh, S. J. Barrow, M. D. Dickey, K. Kalantar-Zadeh, *Chem. Soc. Rev.* **2018**, *47*, 4073; b) A. Goff, P. Aukarasereenont, C. K. Nguyen, R. Grant, N. Syed, A. Zavabeti, A. Elbourne, T. Daeneke, *Dalton Trans.* **2021**, *50*, 7513.

[35] a) N. Cabrera, N. F. Mott, *Rep. Prog. Phys.* **1949**, *12*, 163; b) L. Castilla-Amorós, D. Stoian, J. R. Pankhurst, S. B. Varandili, R. Buonsanti, *J. Am. Chem. Soc.* **2020**, *142*, 19283; c) C. A. Echeverria, J. Tang, Z. Cao, D. Esrafilzadeh, K. Kalantar-Zadeh, *ACS Appl. Nano Mater.* **2022**, *5*, 6820.

[36] F. Hoshyargar, J. Crawford, A. P. O'Mullane, *J. Am. Chem. Soc.* **2017**, *139*, 1464.

[37] N. F. Mott, *Trans. Faraday Soc.* **1940**, *35*, 472.

[38] a) W. M. Saltman, N. H. Nachtrieb, *J. Electrochem. Soc.* **1953**, *100*, 126; b) M. D. Arning, S. D. Minteer, in *Handbook of Electrochemistry* (Ed: C. G. Zoski), Elsevier, Amsterdam **2007**, 813.

[39] E. Gioffredi, M. Boffito, S. Calzone, S. M. Giannitelli, A. Rainer, M. Trombetta, P. Mozetic, V. Chiono, *Proc. CIRP* **2016**, *49*, 125.
[40] a) J. C. Gilbert, J. Hadgraft, A. Bye, L. G. Brookes, *Int. J. Pharm.* **1986**, *32*, 223; b) Y. Yang, J. Wang, X. Zhang, W. Lu, Q. Zhang, *J Control Release* **2009**, *135*, 175; c) M. Guzmán, F. F. García, J. Molpeceres, M. R. Aberturas, *Int. J. Pharm.* **1992**, *80*, 119; d) J.-M. Brunet-Maheu, J. C. Fernandes, C. A. De Lacerda, Q. Shi, M. Benderdour, P. Lavigne, *J. Biomater. Appl.* **2009**, *24*, 275; e) S. F. Khattak, S. R. Bhatia, S. C. Roberts, *Tissue Eng.* **2005**, *11*, 974.
[41] a) Y. Liu, C.-H. Liu, T. Debnath, Y. Wang, D. Pohl, L. V. Besteiro, D. M. Meira, S. Huang, F. Yang, B. Rellinghaus, M. Chaker, D. F. Perepichka, D. Ma, *Nat. Commun.* **2023**, *14*, 541; b) Y. Sun, Y. Xia, *Science* **2002**, *298*, 2176.
[42] a) S. S. Sangaru, H. Zhu, D. C. Rosenfeld, A. K. Samal, D. Anjum, J.-M. Basset, *ACS Appl. Mater. Interfaces* **2015**, *7*, 28576; b) M. A. Majeed Khan, S. Kumar, M. Ahamed, S. A. Alrokayan, M. S. Alsalhi, *Nanoscale Res. Lett.* **2011**, *6*, 434.
[43] P. Chirumamilla, S. B. Dharavath, S. Taduri, *Appl. Biochem. Biotechnol.* **2023**, *195*, 353.
[44] a) C. V. Ramana, E. J. Rubio, C. D. Barraza, A. Miranda Gallardo, S. Mcpeak, S. Kotru, J. T. Grant, *J. Appl. Phys.* **2014**, *115*, 043508; b) C. J. Parker, V. Krishnamurthi, K. Zuraiqi, C. K. Nguyen, M. Irfan, F. Jabbar, D. Yang, M. P. Aukarasereenont, E. L. H. Mayes, B. J. Murdoch, A. Elbourne, K. Chiang, T. Daeneke, *Adv. Funct. Mater.* **2023**, 2304248.
[45] Z. Huang, H. Jiang, P. Liu, J. Sun, D. Guo, J. Shan, N. Gu, *J. Mater. Chem. A* **2015**, *3*, 1925.
[46] a) S. Y. C. Tong, J. S. Davis, E. Eichenberger, T. L. Holland, V. G. Fowler Jr., *Clin. Microbiol. Rev.* **2015**, *28*, 603; b) S. Qin, W. Xiao, C. Zhou, Q. Pu, X. Deng, L. Lan, H. Liang, X. Song, M. Wu, *Signal Transduct. Targeted Ther.* **2022**, *7*, 199.
[47] Y. Kaneko, M. Thoendel, O. Olakanmi, B. E. Britigan, P. K. Singh, *J. Clin. Invest.* **2007**, *117*, 877.
[48] A. Frei, A. D. Verderosa, A. G. Elliott, J. Zuegg, M. A. T. Blaskovich, *Nat. Rev. Chem.* **2023**, *7*, 202.
[49] S. Cheeseman, A. Elbourne, S. Gangadoo, Z. L. Shaw, S. J. Bryant, N. Syed, M. D. Dickey, M. J. Higgins, K. Vasilev, C. F. Mcconville, A. J. Christofferson, R. J. Crawford, T. Daeneke, J. Chapman, V. K. Truong, *Adv. Mater. Interfaces* **2022**, *9*, 2102113.
[50] a) S. Cheeseman, Z. L. Shaw, J. Vongsvivut, R. J. Crawford, M. F. Dupont, K. J. Boyce, S. Gangadoo, S. J. Bryant, G. Bryant, D. Cozzolino, J. Chapman, A. Elbourne, V. K. Truong, *Molecules* **2021**, *26*, 3890. b) Z. L. Shaw, S. Cheeseman, L. Z. Y. Huang, R. Penman, T. Ahmed, S. J. Bryant, G. Bryant, A. J. Christofferson, R. Orrell-Trigg, C. Dekiwadia, V. K. Truong, J. P. Vongsvivut, S. Walia, A. Elbourne, *J. Mater. Chem. B* **2022**, *10*, 7527.
[51] Z. Movasaghi, S. Rehman, D. I. ur Rehman, *Appl. Spectrosc. Rev.* **2008**, *43*, 134.
[52] G. Nahler, in *Dictionary of Pharmaceutical Medicine*, Springer, Vienna **2009**.
[53] A. J. Ridley, M. A. Schwartz, K. Burridge, R. A. Firtel, M. H. Ginsberg, G. Borisy, J. T. Parsons, A. R. Horwitz, *Science* **2003**, *302*, 1704.
[54] J.-L. Wang, J.-K. Xu, C. Hopkins, D. H.-K. Chow, L. Qin, *Adv. Sci.* **2020**, *7*, 1902443.
[55] a) B. Zberg, P. J. Uggowitzer, J. F. Löffler, *Nat. Mater.* **2009**, *8*, 887; b) W. Xu, N. Birbilis, G. Sha, Y. Wang, J. E. Daniels, Y. Xiao, M. Ferry, *Nat. Mater.* **2015**, *14*, 1229.
[56] Y. Yu, H. Lu, J. Sun, *Acta Biomater.* **2018**, *71*, 215.
[57] D. P. Lew, F. A. Waldvogel, *Lancet* **2004**, *364*, 369.
[58] E. A. Masters, B. F. Ricciardi, K. L. D. M. Bentley, T. F. Moriarty, E. M. Schwarz, G. Muthukrishnan, *Nat. Rev. Microbiol.* **2022**, *20*, 385.
[59] N. Kavanagh, J. Ryan Emily, A. Widaa, G. Sexton, J. Fennell, S. O'Rourke, C. Cahill Kevin, J. Kearney Cathal, J. O'Brien Fergal, W. Kerrigan Steven, *Clin. Microbiol. Rev.* **2018**, *37*, 84.
[60] M. Dudareva, A. J. Hotchen, J. Ferguson, S. Hodgson, M. Scarborough, B. L. Atkins, M. A. Mcnally, *J. Infect.* **2019**, *79*, 189.
[61] C. Chai, P. Zhang, L. Ma, Q. Fan, Z. Liu, X. Cheng, Y. Zhao, W. Li, J. Hao, *Bioact. Mater.* **2023**, *25*, 541.
[62] P. P. Spicer, J. D. Kretlow, S. Young, J. A. Jansen, F. K. Kasper, A. G. Mikos, *Nat. Protoc.* **2012**, *7*, 1918.
[63] a) M. C. Biesinger, *Appl. Surf. Sci.* **2022**, *597*, 153681; b) H. Hantsche, *Adv. Mater.* **1993**, *5*, 778.
[64] I. D. Joshipura, C. K. Nguyen, C. Quinn, J. Yang, D. H. Morales, E. Santiso, T. Daeneke, V. K. Truong, M. D. Dickey, *iScience* **2023**, *26*, 106493.
[65] A. Ravindran Girija, S. Balasubramanian, R. Bright, A. J. Cowin, N. Goswami, K. Vasilev, *ChemNanoMat* **2019**, *5*, 1176.
[66] J. Vongsvivut, D. Pérez-Guaita, B. R. Wood, P. Heraud, K. Khambatta, D. Hartnell, M. J. Hackett, M. J. Tobin, *The Analy.* **2019**, *144*, 3226.